MULTINUCLEON TRANSFER FOR ^{160}Gd + ^{186}W COLLISIONS IN THE STOCHASTIC MEAN-FIELD APPROACH

A THESIS SUBMITTED TO
THE GRADUATE SCHOOL OF NATURAL AND APPLIED SCIENCES
OF
MIDDLE EAST TECHNICAL UNIVERSITY

BY

EDA ERBAYRI

IN PARTIAL FULFILLMENT OF THE REQUIREMENTS
FOR
THE DEGREE OF MASTER OF SCIENCE
IN
PHYSICS

SEPTEMBER 2024

Approval of the thesis:

MULTINUCLEON TRANSFER FOR ^{160}Gd + ^{186}W COLLISIONS IN THE STOCHASTIC MEAN-FIELD APPROACH

submitted by **EDA ERBAYRI** in partial fulfillment of the requirements for the degree of **Master of Science in Physics Department, Middle East Technical University** by,

Prof. Dr. Naci Emre Altun
Dean, Graduate School of **Natural and Applied Sciences** _____

Prof. Dr. Seçkin Kürkcüoğlu
Head of Department, **Physics** _____

Prof. Dr. Osman Yılmaz
Supervisor, **Department of Physics, METU** _____

Prof. Dr. Şakir Ayık
Co-supervisor, **Physics Dept., Tennessee Tech University** _____

Examining Committee Members:

Prof. Dr. Bülent Yılmaz
Department of Physics, Ankara University _____

Prof. Dr. Osman Yılmaz
Department of Physics, METU _____

Prof. Dr. Gürsevil Turan
Department of Physics, METU _____

Date:06.09.2024

I hereby declare that all information in this document has been obtained and presented in accordance with academic rules and ethical conduct. I also declare that, as required by these rules and conduct, I have fully cited and referenced all material and results that are not original to this work.

Name, Surname: Eda Erbayri

Signature :

ABSTRACT

MULTINUCLEON TRANSFER FOR ^{160}GD + ^{186}W COLLISIONS IN THE STOCHASTIC MEAN-FIELD APPROACH

Erbayri, Eda
M.S., Department of Physics
Supervisor: Prof. Dr. Osman Yılmaz
Co-Supervisor: Prof. Dr. Şakir Ayık

SEPTEMBER 2024, 59 pages

In deep-inelastic collisions of the heavy-ion systems, projectile and target nuclei stick and move together for a long time, a window opens between the two nuclei and the transfer of nucleons takes place between colliding nuclei. Finally, the system can split into two separate nuclei with different values of initial proton and neutron numbers. If nucleon transfer is from heavy to light, it is called quasi-fission (QF) or light to heavy, called inverse quasifission (IQF). QF and IQF mechanisms are important for the synthesis of heavy elements by multinucleon transfer mechanisms. In this thesis, QF and IQF are studied in the ^{160}Gd + ^{186}W system at two different initial energies. Since both nuclei are deformed, contributions from different initial orientations are calculated, and compared with the experimental data. Multinucleon transfer reaction (MNT) is a way to produce new neutron-rich heavy nuclei. An inverse quasi-fission process may be a possible way to produce yet-unknown superheavy nuclei. The multinucleon transfer mechanism in ^{160}Gd + ^{186}W collisions are investigated in the framework of quantal transport description, based on the stochastic mean-field (SMF) approach. The SMF theory provides a microscopic approach to nuclear dy-

namics beyond the time-dependent Hartree-Fock approach by including mean-field fluctuations. Cross sections for the primary fragment production are determined in the quantal transport description and compared with the available data. In addition, the distributions of cross sections for the production of nuclei with the magic number N=126 are calculated. It is understood that the MNT reactions are a useful process in the production of neutron-rich nuclei in the region close to lead.

Keywords: Stochastic Mean-Field Theory, Time-Dependent Hartree-Fock Theory, Multinucleon Transfer Mechanism, Low Energy Heavy-Ion Reactions

ÖZ

STOKASTİK ORTALAMA ALAN YAKLAŞIMINDA ^{160}Gd + ^{186}W ÇARPIŞMALARI İÇİN ÇOKLU NÜKLEON TRANSFERİ

Erbayri, Eda
Yüksek Lisans, Fizik Bölümü
Tez Yöneticisi: Prof. Dr. Osman Yılmaz
Ortak Tez Yöneticisi: Prof. Dr. Şakir Ayık

Eylül 2024 , 59 sayfa

Ağır iyon sistemlerinin derin elastik olmayan çarpışmalarında, mermi ve hedef çekirdekleri uzun süre birbirine yapışır ve hareket eder. İki çekirdek arasında bir pencere açılır ve çarpışan çekirdekler arasında nükleon transferi gerçekleşir. Son olarak, sistem farklı başlangıç proton ve nötron sayılarına sahip iki ayrı çekirdeğe bölünebilir. Nükleon transferi ağırdan hafife doğruysa buna yarı fisyon (QF), hafiften ağıra doğruysa buna ters yarı fisyon (IQF) denir. QF ve IQF mekanizmaları, çoklu nükleon transfer mekanizmasıyla ağır elementlerin sentezi için önemlidir. Bu tezde, QF ve IQF, ^{160}Gd + ^{186}W sisteminde iki farklı başlangıç enerjisinde incelendi. Her iki çekirdek de deforme olduğundan, farklı başlangıç yönelimlerinden gelen katkılar hesaplandı ve deneysel verilerle karşılaştırıldı. Çoklu nükleon transfer reaksiyonu, nötron açısından zengin yeni ağır çekirdekler üretmenin bir yoludur. Ters yarıfisyon süreci henüz bilinmeyen süper ağır çekirdekler üretmenin olası bir yolu olabilir. ^{160}Gd + ^{186}W çarpışmalarındaki çoklu nükleon transfer mekanizması, stokastik ortalama alan (SMF) yaklaşımına dayalı kuantum mekaniksel tanımı çerçevesinde

araştırıldı. SMF teorisi, ortalama alan dalgalanmalarını dahil ederek zamana bağlı Hartree-Fock yaklaşımının ötesinde nükleer dinamiklere mikroskopik bir yaklaşım sağlar. Birincil reaksiyon ürünlerinin üretimi için tesir kesitleri hesaplandı ve mevcut verilerle karşılaştırıldı. Ek olarak, N=126 sihirli sayılı çekirdeklerin üretimi için tesir kesit dağılımları hesaplandı. MNT reaksiyonlarının kurşuna yakın bölgede nötron açısından zengin çekirdeklerin üretiminde yararlı bir mekanizma olduğu anlaşıldı.

Anahtar Kelimeler: Stokastik Ortalama Alan Kuramı, Zamana Bağlı Hartree-Fock Kuramı, Çoklu Nükleon Transfer Mekanizması, Düşük Enerjili Ağır İyon Reaksiyonları

To my mother, who always believes in me,

to my father, who always be there for us.

ACKNOWLEDGMENTS

Throughout my graduate study, I was extremely lucky to have such helpful, sincere, and supportive people. My academic advisor Prof. Dr. Osman Yılmaz was the one person of all these helpful people who always believed in me even when I quit believing in myself. This work would not have been done without his support. His academic guide and motivational boost helped to complete this journey more peacefully.

I would like to acknowledge Prof. Dr. Şakir Ayık for sharing his knowledge and experience. I also would like to thank Prof. Dr. Sait Umar for sharing his computational experience and sharing the TDHF code.

I was also lucky to work with Mert Arık and Arda Kayaalp who have helped me in every aspect of this work, and I would not be any more appreciative of their aid.

I would like to express my deepest appreciation to my wonderful family, Şeyda Erbayri, Ali İhsan Erbayri, and Berat Erbayri. I could not have completed this journey if it was not for them. Words can not express my gratitude to my mum and Tata for always being behind me, by my side, and with me. I also would like to express my gratitude to Karaböcük for helping me to become the person I am today.

I also want to thank Efekan for supporting all the decisions I make. I am wholeheartedly grateful for you.

I acknowledge that this project is partially supported by the Scientific and Technological Research Council of Turkey, TUBITAK, with Grant No. 122F150.

TABLE OF CONTENTS

ABSTRACT v

ÖZ vii

ACKNOWLEDGMENTS x

TABLE OF CONTENTS xi

LIST OF TABLES xiii

LIST OF FIGURES xiv

LIST OF ABBREVIATIONS xvii

CHAPTERS

1 INTRODUCTION 1

2 MULTINUCLEON TRANSFER MECHANISM BASED ON TDHF THEORY 7

2.1 Hartree-Fock Theory (HF) 8

2.2 The Time-Dependent Hartree-Fock Theory (TDHF) 11

3 MULTINUCLEON TRANSFER MECHANISM BASED ON SMF THEORY 13

3.1 Nucleon Transfer Mechanism 13

3.2 Quantal Diffusion Coefficients 17

3.3 Quantal Drift Coefficients and Curvature Parameters 20

3.4 Cross-section of the Primary Products 23

4 RESULTS 27

4.1 TDHF Results 27

4.1.1 Nucleon Transfer Rate due to Initial Conditions 28

4.1.2 The Calculation in ^{160}Gd + ^{186}W System 32

4.1.3 Calculations of Drift Path and Reduced Curvature Parameters . 35

4.2 SMF Results 44

4.2.1 ^{160}Gd + ^{186}W System at $E_{\text{cm}} = 502.6$ MeV 44

4.2.2 ^{160}Gd + ^{186}W System at $E_{\text{cm}} = 461.9$ MeV 47

5 CONCLUSION 51

REFERENCES 55

LIST OF TABLES

TABLES

Table 4.1 TDHF results for the ^{160}Gd + ^{186}W system at E_{cm} = 502.6 MeV in tip-tip (XX), tip-side (XY), side-tip (YX) and side-side (YY) geometries. 36

Table 4.2 TDHF results for the ^{160}Gd + ^{186}W system at E_{cm} = 461.9 MeV in tip-tip (XX) and tip-side (XY) geometries. 37

Table 4.3 Calculated curvature parameter β. 39

Table 4.4 Calculated curvature parameter α. 43

Table 4.5 SMF results for the ^{160}Gd + ^{186}W reaction at $E_{\text{cm}} = 502.6$ MeV in tip-tip (XX), tip-side (XY), side-tip (YX) and side-side (YY) orientations. 44

Table 4.6 Results of SMF calculations for the ^{160}Gd + ^{186}W reaction at $E_{\text{cm}} = 461.9$ MeV. 48

LIST OF FIGURES

FIGURES

Figure 1.1 The table of nuclides. The figure was taken from Ref. [3]. 2

Figure 1.2 Heavy ion reactions schematic trajectories. The figure was taken from Ref.[20]. 3

Figure 2.1 The target and projectile nuclei illustration for HF computation (a), and the TDHF computation (b). The figure was taken from Ref.[30]. 11

Figure 2.2 The schematic representation of the approach that is used to specify the position and relative wave vector in the TDHF method. The figure was taken from Ref.[30]. 12

Figure 3.1 Geometrical description of the di-nuclear system. The figure was taken from [27]. 14

Figure 3.2 Illustration of isoscalar and isovector drift path. 22

Figure 4.1 The evolution of the proton (Z) and neutron (N) numbers in terms of center of mass energy (E_{cm}), (a) for ^{160}Gd (b) for ^{186}W in tip-tip (XX) geometry. 29

Figure 4.2 The evolution of the proton (Z) and neutron (N) numbers in terms of center of mass energy (E_{cm}). (a) for ^{160}Gd (b) for ^{186}W in tip-side (XY) geometry. 30

Figure 4.3 The evolution of the proton (Z) and neutron (N) numbers in terms of center of mass energy (E_{cm}), (a) for ^{160}Gd (b) for ^{186}W nuclei in side-tip (YX) geometry. 31

Figure 4.4 The evolution of the proton (Z) and neutron (N) numbers in terms of center of mass energy (E_{cm}), (a) for ^{160}Gd (b) for ^{186}W in side-side (YY) geometry. 32

Figure 4.5 The evolution of the proton (Z) and neutron (N) numbers as a function of angular momentum ℓ for the nuclei (a) for ^{160}Gd (b) for ^{186}W nuclei. 33

Figure 4.6 Snapshots of density profiles for different geometries at different times of the reaction mechanism. 34

Figure 4.7 Mean values of proton and neutron numbers for W-like fragmenets in the head-on collision of the ^{160}Gd+^{186}W system at $E_{\text{cm}} = 502.6$ MeV in tip-tip (a), tip-side (b), side-tip (c), and side-side (d) orientations. The figure was taken from Ref.[17] 37

Figure 4.8 The drift path of W-like fragments in head-on collisions of the system ^{160}Gd + ^{186}W at $E_{\text{cm}} = 502.6$ MeV in tip-tip (a), tip-side (b), side-tip (c), and side-side (d) orientations. The figure was taken from Ref.[17] 38

Figure 4.9 The neutron and proton diffusion coefficients of the ^{160}Gd+^{186}W system at $E_{\text{cm}} = 502.6$ MeV in tip-tip (a), tip-side (b), side-tip (c), and side-side (d) geometries. The figure was taken from Ref.[17] 40

Figure 4.10 Mean values of proton and neutron numbers in the head-on collision of the ^{172}Gd + ^{174}W at $E_{\text{cm}} = 502.6$ MeV in tip-tip (a), tip-side (b), side-tip (c), and side-side (d) orientations. The figure was taken from Ref.[17] 41

Figure 4.11 The drift path of W-like fragments in head-on collisions of the system ^{172}Gd + ^{174}W at $E_{\text{cm}} = 502.6$ MeV in tip-tip (a), tip-side (b), side-tip (c), and side-side (d) orientations. The figure was taken from Ref.[17] 42

Figure 4.12 The neutron and proton diffusion coefficients of the system ^{172}Gd+ ^{174}W at $E_{\text{cm}} = 502.6$ MeV in tip-tip (a), tip-side (b), side-tip (c), and side-side (d) geometries. The figure was taken from Ref.[17] 43

Figure 4.13 Neutron, proton, and mixed variances as a function of time in head-on collisions of the system ^{160}Gd + ^{186}W system at $E_{\text{cm}} = 502.6$ MeV in tip-tip (a), tip-side (b), side-tip (c), and side-side (d) geometries. The figure was taken from [17]. 45

Figure 4.14 Total cross-sections of the system ^{160}Gd+ ^{186}W system at $E_{\text{cm}} = 502.6$ MeV as a function of mass number A. The red dashed lines indicate the tip-tip, dotted-green lines tip-side, dashed-dotted purple lines side-tip, and dotted-dashed blue lines indicates the collision geometry of side-side reactions. Mean cross-section and experimental data are taken from Ref.[41] and are indicated by the solid black lines and yellow triangles, respectively. The figure was taken from Ref.[17] 46

Figure 4.15 The cross-sections of primary products of the system ^{160}Gd + ^{186}W system at $E_{\text{cm}} = 502.6$ MeV. The figure was taken from Ref.[17]. . 47

Figure 4.16 Total cross-section of the system ^{160}Gd + ^{186}W system at $E_{\text{cm}} = 461.9$ MeV as a function of mass number A. The red dashed lines represent the tip-tip, dotted-green lines tip-side. The figure was taken from [17]. Mean cross-section and experimental data are taken from Ref.[41] are indicated by the solid black lines and yellow circles, respectively. The figure was taken from Ref.[17]. 49

LIST OF ABBREVIATIONS

ABBREVIATIONS

2D	2 Dimensional
SHE	Super Heavy Element
MNT	Multinucleon Transfer
QF	Quasi-Fission
FF	Fusion-Fission
IQF	Inverse Quasifission
HF	Hartree-Fock
TDHF	Time-Dependent Hartree-Fock
TDRPA	Time-Dependent Random Phase Approximation
SMF	Stochastic Mean-Field

CHAPTER 1

INTRODUCTION

Ernest Rutherford has been made a breakthrough by finding the core of every atom called atomic nucleus in 1911 [1]. After this leap, the focus of research have been gathered around understanding of the properties of nucleus, type of forces, and the concept of discovering elements. The nucleus consists of nucleons which are protons and neutrons. Fig. 1.1 shows the chart of nuclides, also known as the Segrè chart. It is first published by Kurt Guggenheimer in 1934, and expanded by Giorgio Fea in 1935, Emilio Segrè in 1945 [2]. The Segrè chart is a 2 dimensional (2D) graph, the horizontal axis represents the neutron number (N), the vertical axis represents the proton number (Z). The horizontal rows of the nuclides are the same elements which have the same Z, and different N. These elements are called isotopes.

Understanding the properties of the nucleus and the type of nuclear reactions has helped expand the chart. There is still a considerably large amount of area consisting of unknown isotopes. 286 initial isotopes exist naturally on Earth [4], but after the progress of understanding nuclear reactions, the findings of unknown isotopes have accelerated, and findings have reached up to 3000 [4]. Presently, the predictions have indicated that there are still unknown 4000 isotopes [5],[6] that can be produced experimentally with fragmentation, fusion, fission and multinucleon transfers [7].

The top-right side of Fig. 1.1 consists of the most challenging area for the production of isotopes both experimentally and theoretically [8],[9],[10],[11],[12]. The most common approach for synthesizing the super heavy elements (SHE) and their isotopes is the fusion reactions. The first experimentally applied approaches are divided into two groups as hot fusion and cold fusion [13].

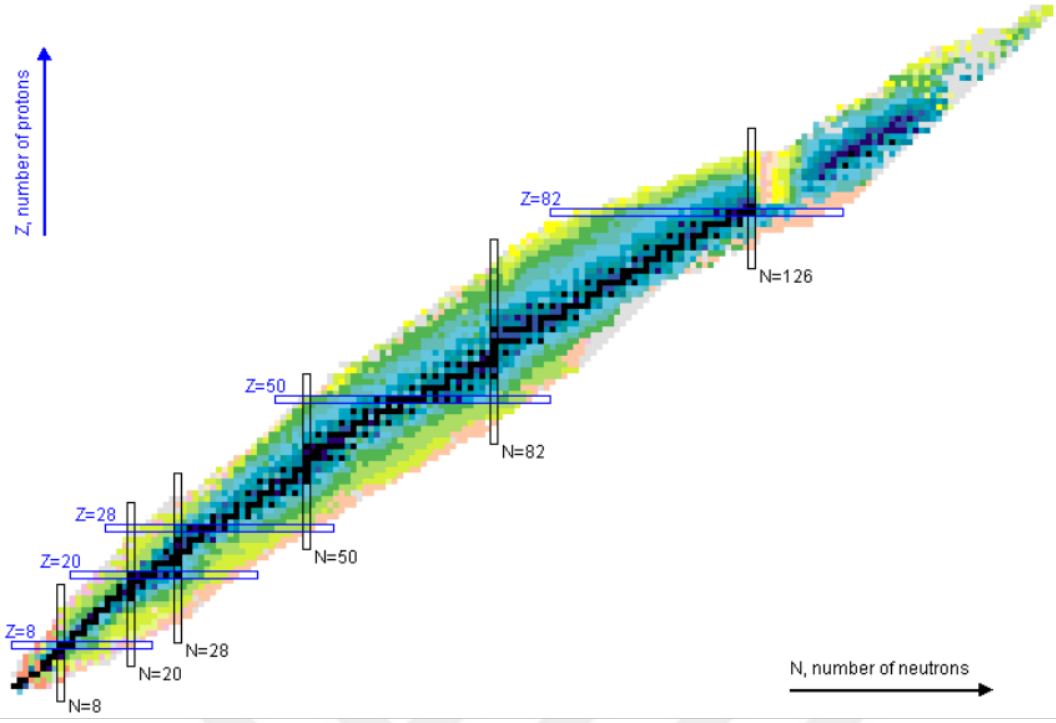


Figure 1.1: The table of nuclides. The figure was taken from Ref. [3].

The primary products that comes from these processes have a comparatively high excitation energy, and they tend to make a secondary fission and return to lower energy levels by emitting alpha particles, and neutrons [14]. Since the process is left with a significantly small evaporation residue cross section, the production of heavy elements including neutron-rich ones is hard to achieve. Therefore, it can be stated that the hot and cold fusion are limited for the production of heavy elements, and a new perspective should be used for further improvements [15]. At this stage, multinucleon transfer is stated as a promising alternative for synthesizing the heavy elements. Recently, the focus of the research have become using the actinide targets at near Coulomb barrier energies so that the production of the primary products is achieved at reasonably low excitation energies [16]. This property have influence the use of multinucleon transfer (MNT) over the fusion, fission and fragmentation processes [17].

This thesis focusses on heavy ion reactions that are known as the ions heavier than the helium nucleus. The elements heavier than Plutonium, which has the atomic number of 94, are unstable, and they are produced artificially [18]. Also, the elements that

have bigger atomic number than 104 are called super heavy elements. Super heavy elements with atomic numbers bigger than 118 are produced by the fusion reaction, but cross-section of these reactions are quite small [19]. Therefore, it is important to understand the behaviour of the reaction when parameters change. Here, the referred to parameters are the collision energy, symmetry, shell structure and deformation of nuclei. The heavy ion reactions can be separated in view of the bombarding energy per nucleon in three groups. The first group is the low energy (10 MeV/nucleon), the second one is the medium energy (100 MeV/nucleon – 1GeV), and the last group is the high energy reactions (larger than 1GeV). The low energy heavy ion collisions can be classified according to the impact parameter (b) of the collision which is defined as the perpendicular distance between the path of the projectile and center of the target.

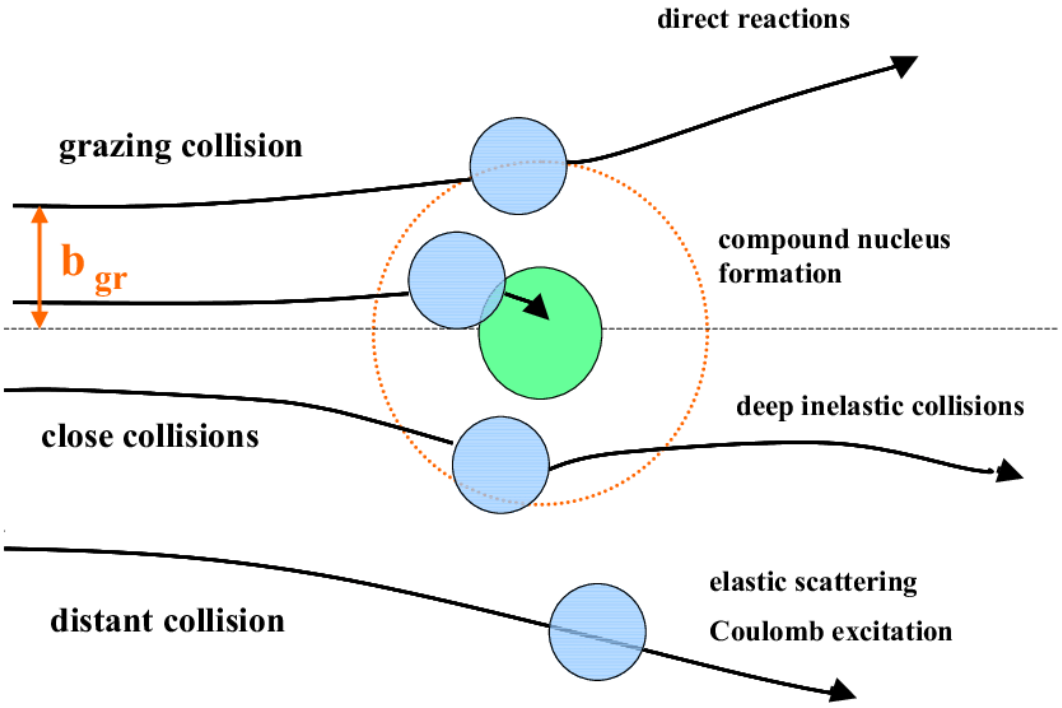


Figure 1.2: Heavy ion reactions schematic trajectories. The figure was taken from Ref.[20].

Fig. 1.2 illustrates the trajectories of the heavy ion reactions. In the case of distant collision, the nuclear interaction can be neglected, and only the Coulomb excitation determines the trajectory of the collision, so the collision will be elastic. On the other hand, for the grazing collision, there may be a transaction of nucleons between the

two nuclei, or nucleons may react directly to excited levels and break off from the nucleus, and it is known as the inelastic collision. If the impact parameter (b) decreases to a level that is sufficiently low or zero (called head-on collision), the whole kinetic energy of the projectile nucleus is shared between the nucleons, and it merges to a single unstable nucleus, but it decays in a short time. It is known as the fusion. In the heavy-ion fusion reactions one nuclei is fixed at a point, and it is called target nuclei. Other nuclei which are sent to the target are called projectile. Usually, the lighter nuclei are chosen as projectile. The fusion reaction between them occurs in three steps. First, the projectile nuclei are sent to the target nuclei, and after it passes through the Coulomb barrier, it coheres with the target. Second, the cohered system reaches the thermal balance and forms a compound nucleus. For the final part, a joined system that is in the excited state goes through the fusion-fission reaction or emits particles such as; neutron, proton, and alpha. This event is called evaporation. It is known that the super heavy elements (SHE) are the fusion products by synthesizing the evaporation residue. As the impact parameter decreases, the nuclear interaction effect becomes bigger, and the nucleon exchange will increase. Some part of the kinetic energy of the projectile nucleus is shared while the system is moving, and in the end, they split. This kind of reaction is called a deep inelastic collision. The interest of this thesis focuses on the deep inelastic heavy-ion collisions at low energy near the Coulomb barrier. The motion occurs as the system separates into two fragments without fusing one another, and it is called quasifission (QF). When the di-nuclear system separates into fragments, the following options may occur. One is QF, and the other is called fusion-fission (FF) reaction. In the FF process, the projectile and the target nuclei stick together and forms a compound nucleus. This excited compound nucleus deexcites by fission reaction, for this reason the process is called FF. The deexcitation event takes place as the compound nucleus evaporates proton, neutron and alpha particles to the point where the evaporation residue is formed. The difference between them is the contact time. For the QF, the contact time is less than the FF reaction. This long contact time makes the charge and mass transfer of the nuclei much more. It can be stated that in the QF reaction, the nucleon transfer is significantly high between the colliding particles, and this transfer is usually from the side of the heavy particle to the light one. On the other hand, it is proved that in a process called inverse quasifission (IQF) the light ions can transfer nucleons to the heavier

ones. This phenomenon has become an essential tool to reach the unknown part of the chart that consists of an exceptional property of heavy ion reactions. Between the centers, a window forms, and through this window, nucleon transfer occurs while conserving the total mass number. On the other hand, there may be formed two separate nucleons with different proton and neutron numbers from their initials. While these nucleons are forming, the nucleon transfer between them shows the reaction behavior. Therefore, to understand the evolution of the transfer, some transport models of macroscopic variables are considered. With these methods, the potential energy of the system and transport coefficients are computed empirically. Also, to calculate the nucleon transfer, the empirical models of Langevin equations are presented. At this point, time-dependent Hartree-Fock (TDHF) theory are used to determine the mean values of collective variables evolution. This theory is limited to considering the reaction mechanism in the mean field approach. Therefore, the quantal and thermal fluctuations can not computed with TDHF theory. At this point, Balian and Veneroni developed an approach to take into account the variances of collective variables, and it is called time-dependent random phase approximation (TDRPA) [21]. With this approach, a single Slater determinant is used to define the variances of single-particle distributions. However, the current form of the TDRPA approach can not be applied to asymmetric systems. Since there is difficulty of numerical calculations in asymmetric systems, the applications are limited. It is understood that there is a need of going beyond the standard mean-field approach. The stochastic mean field approach considers the fluctuations beyond the correlations. It can also be applied to asymmetric systems and coincides with the TDRPA approach in the limit of small fluctuations. With the help of the stochastic mean field (SMF) approach, the quantal and thermal density fluctuations are considered. Therefore, the SMF approach provides a microscopic framework for the diffusion mechanism. The evolution of the macroscopic variables occurs in terms of the generalized Langevin description of the quantal transport process [22]. With the help of the SMF approach, not only quantal effects are considered, but also the memory effect and collision geometry are included to obtain the reaction behavior.

Obtaining new neutron-rich heavy and super heavy nuclei is the main focus of this thesis. The energies near the Coulomb barrier provide the lowest excitation energies

to the primary fragments, giving them a chance to survive without having a fission process[23]. Determining unknown neutron-rich heavy nuclei at near Coulomb barrier energies are increasing the yield of fragments in the region of proton and neutron shells in terms of the effect of the closed shell properties [24]. The calculations are made in the region of Ba and Pb, and it is shown that the yield of the fragments is increasing between the collisions of ^{160}Gd + ^{186}W nuclei. Also, it is experimentally shown that the effect of proton shells Z=28 and Z=82, between the collision partners of ^{88}Sr and ^{176}Yb the yield of the fragments have increased near Coulomb barrier energies [25]. According to these experimental insights, in this thesis ^{160}Gdand^{186}W nuclei are studied by using MNT reactions in the region close to lead to synthesize neutron-rich nuclei.

CHAPTER 2

MULTINUCLEON TRANSFER MECHANISM BASED ON TDHF THEORY

The MNT mechanism in heavy-ion collisions is used to understand the production of SHE with the help of Hartree-Fock (HF) and time-dependent Hartree-Fock (TDHF) theory [26]. The static properties of the colliding nucleus are determined with HF theory. In the HF theory, the wave function is used as a single Slater determinant in terms of a single particle wave function. In this way, the N-particle Schrödinger equations are reduced to N-particle non-linear differential equations. Therefore, the picture becomes as the equations of the individual particles moving in the mean potential which is produced by all particles in the system. Overall, this approximation is called the mean-field approach. TDHF theory has been the primary microscopic tool to understand the behavior of heavy-ion collisions and fusion reactions. It is the extended version of the static time-dependent HF approach. Since the TDHF equation is the first-order differential equation, the many-body wave function is determined with an initial condition after the time evolution. The most probable collision path of quantum many-body action at low energy heavy ion collisions is given as an output of the theory. Given a set of initial conditions to the system, the output of the theory is a single path. Altering the initial conditions, such as; angular momentum or orientation of the target and projectile nuclei, the distribution of the reaction can be determined. The one-body system dissipation is well explained by using TDHF, but for multiple mass and charge distribution the theory needs an upgrade [27].

2.1 Hartree-Fock Theory (HF)

The nucleus is considered as a group of non-interacting nucleons moving in a mean-field potential. This kind of approach provides decent outputs for nuclear processes. However, finding such a potential is questionable. With the help of nuclear forces and the Pauli exclusion principle, one can construct the mean-field potential. In the HF theory, the potential is derived from the Skyrme interaction. Therefore, the static HF approach is used to compute the ground state properties of nuclei. The HF method is an approximate approach for obtaining the ground-state wave function and ground-state energy. Using the single Slater determinant provides the approximation for the many-body wave function. The derivation of coupled equations for the many-body system is held by using the variational principle. The HF wave functions and energy of the system are constructed via the solution of these equations. In HF theory, the ground state wave function of the nucleus is represented by the single Slater determinant [28] which is obtained from the single particle state wave functions $\phi_i(r_i)$, and it is known as the Hartree-Fock state.

$$\Phi\left(r_1 \ldots r_A\right) \rightarrow \Phi_{HF}\left(r_1 \ldots r_A\right) = \frac{1}{\sqrt{A!}} \begin{vmatrix} \phi_1\left(r_1\right) & \phi_1\left(r_2\right) & \cdots & \phi_1\left(r_A\right) \\ \phi_2\left(r_1\right) & \phi_2\left(r_2\right) & \cdots & \phi_2\left(r_A\right) \\ \vdots & \vdots & \ddots & \vdots \\ \phi_A\left(r_1\right) & \phi_A\left(r_2\right) & \cdots & \phi_A\left(r_A\right) \end{vmatrix} . \quad (2.1)$$

where r denotes the space, spin, and iso-spin coordinates.

The many-body Hamiltonian is represented as,

$$\hat{H} = \sum_{i=1}^{A} \frac{\hat{p}_i^2}{2m_i} + \frac{1}{2} \sum_{i \neq j}^{A} V\left(r_i, r_j\right) . \quad (2.2)$$

where $V(r_i, r_j)$ consists of all parts of the nucleon-nucleon force including the Coulomb interaction [28]. The approximation of the ground state energy is computed with the

expectation value of the Hamiltonian.

$$\begin{aligned} E^0 &= \left\langle \Phi \left| \hat{H} \right| \Phi \right\rangle \\ &= -\frac{\hbar^2}{2m} \sum_{i=1}^{A} \int \phi_i^*(r) \nabla^2 \phi_i(r)\, dr \\ &\quad + \frac{1}{2} \sum_{i \neq j}^{A} \iint \phi_i^*(r) \phi_j^*(r') V(r,r') \phi_i(r) \phi_j(r')\, dr\, dr' \\ &\quad - \frac{1}{2} \sum_{i \neq j}^{A} \iint \phi_i^*(r) \phi_j^*(r') V(r,r') \phi_i(r') \phi_j(r)\, dr\, dr'. \end{aligned} \tag{2.3}$$

With the help of the variational principle, the Eq.2.3 becomes

$$\frac{\delta}{\delta \phi_a^*(r)} \left(E^0 - \sum_{i=1}^{A} \epsilon_i \int |\phi_i(r)|^2\, dr \right) = 0. \tag{2.4}$$

The wave-function is normalized, and the particle number is conserved via Lagrange multipliers, ϵ_i.

$$\sum_{i=1}^{A} \int |\phi_i(r)|^2\, dr = A. \tag{2.5}$$

Eq.2.3, and Eq.2.4 are used to determine the Hartree-Fock equations,

$$\begin{aligned} \epsilon_i \phi_i(r) &= -\frac{\hbar^2}{2m} \nabla^2 \phi_i(r) + \sum_{j>i}^{A} \int \phi_j^*(r') V(r,r') \phi_i(r) \phi_j(r')\, dr' \\ &\quad - \sum_{j>i}^{A} \int \phi_j^*(r') V(r,r') \phi_i(r') \phi_j(r)\, dr'. \end{aligned} \tag{2.6}$$

In the Eq.2.6, the second term is called the Hartree term, and the expression is indicated as;

$$U_H^{(i)}(r) = \sum_{j>i}^{A} \int \phi_j^*(r') V(r,r') \phi_j(r')\, dr'. \tag{2.7}$$

The third term is named as Fock potential,

$$U_F^{(i)}(r,r') = \sum_{j>i}^{A} \phi_j^*(r') V(r,r') \phi_j(r). \tag{2.8}$$

Finally, the simplified expression of the HF equations become

$$\epsilon_i \phi_i(r) = -\frac{\hbar^2}{2m} \nabla^2 \phi_i(r) + U_H^{(i)}(r) \phi_i(r) - \int U_F^{(i)}(r,r') \phi_i(r')\, dr'. \tag{2.9}$$

The solution of the HF equations creates the ground state Slater determinant. The HF equations include the potentials that depend on the wave-function, so it makes the equations nonlinear, and a self-consistent solution is needed. The HF theory provides an approach to derive a single-particle potential from the two-body interaction that depends not only on the coordinates of particles but also on their relative momenta. The Skyrme Hamiltonian is expressed as;

$$\hat{H}_{\text{Skyrme}} = \hat{T} + \sum_{i<j} \hat{v}_{ij} + \sum_{i<j<k} \hat{v}_{ijk} + \hat{V}_{\text{Coul}}. \tag{2.10}$$

where $\hat{T}$ is the kinetic energy operator, and it is shown as;

$$\hat{T} = \sum_{i=1}^{N} \frac{\hat{p}_i^2}{2m}. \tag{2.11}$$

where $\hat{p}_i = -\mathrm{i}\hbar\nabla_i$.$\hat{V}_{\text{Coul}}$ and the Coulomb potential is given by

$$\hat{V}_{\text{Coul}} = \sum_{i<j} \frac{e^2}{|r_i - r_j|} \delta_{q_i p} \delta_{q_j p}. \tag{2.12}$$

.

The Skyrme effective interaction is represented as the two-body density-dependent interaction;

$$\begin{aligned}
\hat{V}_{SK(ij)} = \hat{v}\left(r_i\sigma_i, r_j\sigma_j\right) =& t_0\left(1 + x_0\hat{P}_\sigma\right)\delta\left(r_i - r_j\right) \\
&+ \frac{1}{2}t_1\left(1 + x_1\hat{P}_\sigma\right)\left\{\delta\left(r_i - r_j\right)\hat{k}^2 + \hat{k}'^2\delta\left(r_i - r_j\right)\right\} \\
&+ t_2\left(1 + x_2\hat{P}_\sigma\right)\hat{k}'\cdot\delta\left(r_i - r_j\right)\hat{k} \\
&+ \frac{1}{6}t_3\rho^\alpha\left(\frac{r_i + r_j}{2}\right)\left(1 + x_3\hat{P}_\sigma\right)\delta\left(r_i - r_j\right) \\
&+ \mathrm{i}W_0\left(\hat{\sigma}_i + \hat{\sigma}_j\right)\cdot\left\{\hat{k}'\times\delta\left(r_i - r_j\right)\hat{k}\right\}.
\end{aligned} \tag{2.13}$$

The static properties of the nuclei are obtained by determining the factors t_0, t_1, t_2, t_3, α and W_0. Here, $\hat{k}$ and $\hat{k}'$ are the operators of relative wave vectors that act on the functions right and left, respectively.

$$\hat{k} = \frac{\vec{\nabla}_i - \vec{\nabla}_j}{2\mathrm{i}}, \quad \hat{k}' = -\frac{\overleftarrow{\nabla}_i - \overleftarrow{\nabla}_j}{2\mathrm{i}}. \tag{2.14}$$

2.2 The Time-Dependent Hartree-Fock Theory (TDHF)

The TDHF theory is the time-dependent version of the HF theory. The HF equations are used to derive the TDHF equations in such expression,

$$\frac{\delta}{\partial\phi_a^*(r\sigma,t)}\int <\Phi(t)|\left(i\hbar\frac{\partial}{\partial t}-\hat{H}\right)|\Phi(t)>dt'=0. \tag{2.15}$$

Similarly, the Skyrme Hamiltonian is obtained as;

$$\mathrm{i}\hbar\frac{\partial\phi_i(r,\sigma,t)}{\partial t}=\hat{H}\Phi(r,t). \tag{2.16}$$

where $\phi_i(r\sigma,t)$ is represented as the single-particle wave function of ith particle with spin σ and isospin q at position r [29]. Here, the total energy E is conserved in the action. It is seen that this approximation is a useful approach regarding the analysis of the dynamic processes in heavy-ion collisions.

In this part, the tools that are used to investigate the heavy ion reactions with TDHF theory are presented. Preparing the wave function of the projectile and target nuclei in the HF ground state is mandatory to begin the heavy ion reactions [30].

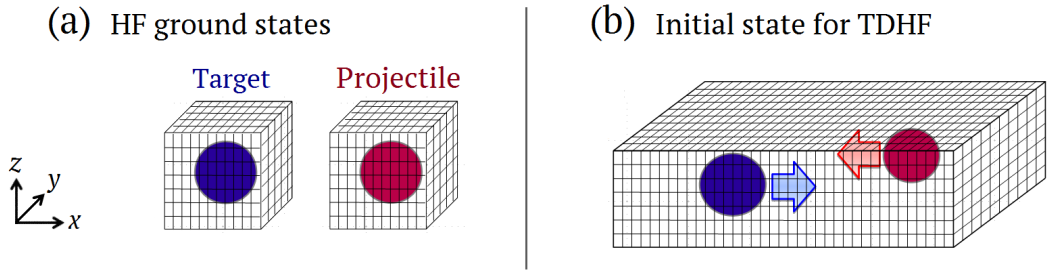


Figure 2.1: The target and projectile nuclei illustration for HF computation (a), and the TDHF computation (b). The figure was taken from Ref.[30].

Fig.2.1 (a) represents the HF part of the simulation of target and projectile nuclei, and Fig.2.1 (b) shows the TDHF part of the calculation for the system. As shown in Fig.2.1, in the HF part of the calculations, the ground states of target and projectile nuclei are computed individually. For the TDHF part, the projectile and target nuclei are put in a rectangular box to calculate the dynamic part of the reaction.

The heavy ion reactions in our work are stimulated by the TDHF theory. To make the computations easier, a finite-sized box is used in our heavy ion reactions. In Fig. 2.2

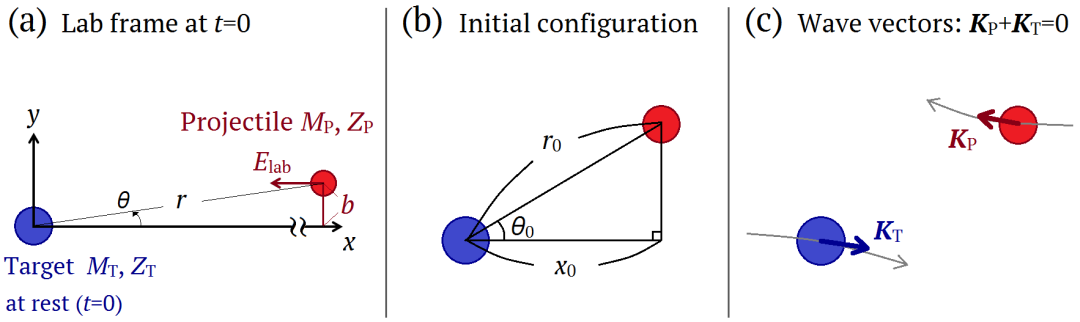


Figure 2.2: The schematic representation of the approach that is used to specify the position and relative wave vector in the TDHF method. The figure was taken from Ref.[30].

(a), an example of a scattering problem is shown. In Fig. 2.2 (b), two nuclei are separated by x_0 distance in x-axis, and in Fig. 2.2 (c), the wave vectors K_T for target and K_P for projectile at initial conditions are represented. The distance between the two nuclei must be shorter than the size of the finite-sized box that we use in our calculations. The two nuclei are set in the finite-sized box such that the Coulomb excitations are neglected before they come to the initial position. Finally, the two nuclei are ready to move in a box. To stimulate the motion, an initial momentum is given to the system, and the process is started.

CHAPTER 3

MULTINUCLEON TRANSFER MECHANISM BASED ON SMF THEORY

One of the upgrades is called time-dependent random phase approximation (TDRPA). This approach is proposed by the Veneroni and Balian, and this method has been used in several research about MNT [31],[32]. For the symmetric collisions, the TDRPA method is sufficient to obtain the charge and mass distributions. Due to the restricted area of TDRPA, as a further improvement, the stochastic mean-field (SMF) approach is suggested [33].

3.1 Nucleon Transfer Mechanism

An ordinary TDHF theory shows the deterministic description of the many-body system. Given an initial condition which is composed of a single Slater determinant, a specific single-particle density matrix is obtained. However, because of the correlations, the accurate initial state should be a superposition of Slater determinants rather than a single Slater determinant. In the view of SMF theory, a set of single-particle density matrices is used to represent the correct initial state. Single particle density matrices are found by considering the initial fluctuations [34]. The set of single particle density matrices is obtained with TDHF equations using a self-consistent Hamiltonian for each event. The fluctuations that form the initial density matrices are obtained by using the Gaussian distribution. The distribution is required to match the set of mean one-body dispersions in the initial state with the quantal view in the mean-field approach. In the scenario of the di-nuclear system being retained as collision dynamics of the heavy-ion collisions near barrier energy, the set of mean field events is not required. In the perspective of the collision dynamics, the properties

of the collision become important. For the use of ease, two colliding nuclei can be stated as target-like and projectile-like. The variables of the particles should be specified by considering the asymmetry of mass and charge of the nuclei, relative distance and momentum, while maintaining the window between the system. The geometrical description of the di-nuclear system is shown in Fig3.1. The central coordinate of the window is located at (x_0, y_0). There θ is the angle between the symmetry axis and collision axis. Window plane is indicated by the red-dashed line.

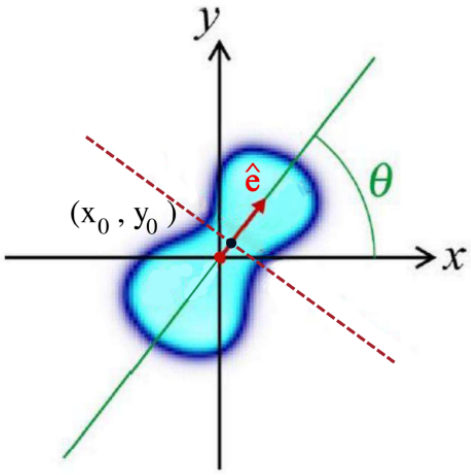


Figure 3.1: Geometrical description of the di-nuclear system. The figure was taken from [27].

Here the x-axis is the collision axis. The symmetry axis and window plane is shown in green line and red-dashed line respectively. The unit vector $\hat{e}$ shows a direction perpendicular to window plane.

The neutron and proton numbers from one side of the window are taken as a macroscopic variable. With the help of the SMF theory, the proton and neutron numbers in terms of the densities of the proton and neutron are given by;

$$\begin{pmatrix} N_1^\lambda(t) \\ Z_1^\lambda(t) \end{pmatrix} = \int d^3r\Theta\left\{[x - x_0(t)]\cos\theta + [y - y_0(t)]\sin\theta\right\} \begin{pmatrix} \rho_n^\lambda(\vec{r}, t) \\ \rho_p^\lambda(\vec{r}, t) \end{pmatrix}. \quad (3.1)$$

Here, θ is the step function. In the SMF theory, the evolution of the variables in time is determined in terms of the Langevin dynamics. The evolution of the proton and neutron numbers of projectile-like nuclei are given by;

$$\frac{d}{dt}\begin{pmatrix} N_1^\lambda(t) \\ Z_1^\lambda(t) \end{pmatrix} = \int d^3r\delta\left(x'\right)\dot{\mathrm{x}}'\begin{pmatrix} \rho_n^\lambda(\vec{\mathrm{r}}, t) \\ \rho_p^\lambda(\vec{\mathrm{r}}, t) \end{pmatrix} + \int d^3r\Theta\left(x'\right)\frac{\partial}{\partial t}\begin{pmatrix} \rho_n^\lambda(\vec{\mathrm{r}}, t) \\ \rho_p^\lambda(\vec{\mathrm{r}}, t) \end{pmatrix}. \quad (3.2)$$

Using the continuity equation of the density ρ and current j as;

$$\frac{\partial}{\partial t}\rho_{\alpha}^{\lambda}(\vec{r},t) = -\vec{\nabla}\cdot\vec{j}_{\alpha}^{\lambda}(\vec{r},t) = -\left[\partial_x j_{x,\alpha}^{\lambda}(\vec{r},t) + \partial_y j_{\mathrm{y},\alpha}^{\lambda}(\vec{r},t) + \partial_z j_{\mathrm{z},\alpha}^{\lambda}(\vec{r},t)\right]. \quad (3.3)$$

we obtain the evolution of proton and neutron numbers as a stochastic Langevin equation,

$$\frac{d}{dt}\begin{pmatrix} N_1(t) \\ Z_1(t) \end{pmatrix} = \int d^3r g\left(x'\right)\begin{pmatrix} \dot{x}'\rho_n(\vec{r},t) + \hat{e}\cdot\vec{j}_n(\vec{r},t) \\ \dot{x}'\rho_p(\vec{r},t) + \hat{e}\cdot\vec{j}_p(\vec{r},t) \end{pmatrix} = \begin{pmatrix} v_n(t) \\ v_p(t) \end{pmatrix}. \quad (3.4)$$

The drift coefficient of the proton $v_p(t)$ and neutron $v_n(t)$ in the event of λ are determined by the current of the proton $j_p(\vec{r},t)$ and neutron $j_n(\vec{r},t)$ in the window. Here instead of using the delta function, the Gaussian distribution can be used for small values of κ in the equation given by;

$$g(x) = \frac{1}{\kappa\sqrt{2\pi}}\exp\left(-x^2/2\kappa^2\right). \quad (3.5)$$

For the numerical calculations, the lattice dimension $\kappa = 1.0$ fm is taken. By taking the mean of the Langevin equations cluster, proton and neutron numbers are obtained. The averaged particle density and the current density are given as;

$$\rho_{\alpha}(\vec{r},t) = \sum_{h\in\alpha}\Phi_h^{*\alpha}(\vec{r},t)\Phi_h^{\alpha}(\vec{r},t), \quad (3.6)$$

$$\vec{j}_{\alpha}(\vec{r},t) = \frac{\hbar}{m}\sum_{h\in\alpha}\mathrm{Im}\left(\Phi_h^{*\alpha}(\vec{r},t)\vec{\nabla}\Phi_h^{\alpha}(\vec{r},t)\right). \quad (3.7)$$

The drift coefficients $v_p(t)$ and $v_n(t)$ are indicated by the net proton and neutron currents near the window plane. The summation of h points to the hole states of the projectile and target nuclei that are occupied with the nucleons. The fluctuations of the mean values of proton and neutron numbers are computed via linearizing the mean values of proton $Z_1(t)$ and neutron $N_1(t)$ numbers. These fluctuations can take place because of two reasons. The first one is the variance in wavefunctions. The second one comes from the initial stochastic fluctuations of the density matrix elements can affect the system as $\delta\rho_{ji}^{\lambda} = \rho_{ji}^{\lambda} - \delta_{ji}n_j$.

The proton and neutron drift coefficients of an ensemble in the event λ are determined by the proton and neutron currents ($\mathrm{v}_p^{\lambda}(t)$ and $\mathrm{v}_n^{\lambda}(t)$) in the window. Also, their fluctuations $\delta\mathrm{v}_p^{\lambda}(t)$, $\delta\mathrm{v}_n^{\lambda}(t)$ are represented by the stochastic expressions of the

currents. When the linearized drift coefficients around their average values and their mean values are used, the Langevin equation becomes

$$\begin{pmatrix} \mathrm{v}_p^{\lambda}(t) \\ \mathrm{v}_n^{\lambda}(t) \end{pmatrix} = \begin{pmatrix} \mathrm{v}_p(t) \\ \mathrm{v}_n(t) \end{pmatrix} + \begin{pmatrix} \frac{\partial \mathrm{v}_p}{\partial Z_1}\left(Z_1^{\lambda} - \overline{Z_1^{\lambda}}\right) + \frac{\partial \mathrm{v}_p}{\partial N_1}\left(N_1^{\lambda} - \overline{N_1^{\lambda}}\right) \\ \frac{\partial \mathrm{v}_n}{\partial Z_1}\left(Z^{\lambda} - \overline{Z_1^{\lambda}}\right) + \frac{\partial \mathrm{v}_n}{\partial N_1}\left(N_1^{\lambda} - \overline{N_1^{\lambda}}\right) \end{pmatrix} + \begin{pmatrix} \delta \mathrm{v}_p^{\lambda}(t) \\ \delta \mathrm{v}_n^{\lambda}(t) \end{pmatrix}. \quad (3.8)$$

The fluctuations $\delta \mathrm{v}_p^{\lambda}(t)$, $\delta \mathrm{v}_n^{\lambda}(t)$ that come from the stochastic parts of the proton and neutron current are uncorrelated Gaussian distributions, and their mean values $\overline{\delta \mathrm{v}_p^{\lambda}(t)}$ and $\overline{\delta \mathrm{v}_n^{\lambda}(t)}$ are held as zero. By using Eq. 3.4, the time evolution of the proton and neutron number fluctuations are given by;

$$\frac{d}{dt}\begin{pmatrix} \delta Z_1^{\lambda}(t) \\ \delta N_1^{\lambda}(t) \end{pmatrix} = \begin{pmatrix} \frac{\partial \mathrm{v}_p}{\partial Z_1}\left(Z_1^{\lambda} - \overline{Z_1^{\lambda}}\right) + \frac{\partial \mathrm{v}_p}{\partial N_1}\left(N_1^{\lambda} - \overline{N_1^{\lambda}}\right) \\ \frac{\partial \mathrm{v}_n}{\partial Z_1}\left(Z^{\lambda} - \overline{Z_1^{\lambda}}\right) + \frac{\partial \mathrm{v}_n}{\partial N_1}\left(N_1^{\lambda} - \overline{N_1^{\lambda}}\right) \end{pmatrix} + \begin{pmatrix} \delta \mathrm{v}_p^{\lambda}(t) \\ \delta \mathrm{v}_n^{\lambda}(t) \end{pmatrix}. \quad (3.9)$$

In the SMF theory, the fluctuations $\delta \mathrm{v}_p^{\lambda}(t)$ and $\delta \mathrm{v}_n^{\lambda}(t)$ are influenced by the stochastic parts of the proton and neutron currents. The mean values of fluctuations are represented as $\overline{\delta \mathrm{v}_p^{\lambda}(t)} = 0$ and $\overline{\delta \mathrm{v}_n^{\lambda}(t)} = 0$. The variances of proton and neutron diffusion coefficients $D_{ZZ}(t)$ and $D_{NN}(t)$ are respectively stated by the Markovian approach [35] as;

$$\overline{\delta \mathrm{v}_p^{\lambda}(t)\delta \mathrm{v}_p^{\lambda}\left(t'\right)} = 2\delta\left(t - t'\right) D_{ZZ}(t), \quad (3.10)$$

$$\overline{\delta \mathrm{v}_n^{\lambda}(t)\delta \mathrm{v}_n^{\lambda}\left(t'\right)} = 2\delta\left(t - t'\right) D_{NN}(t). \quad (3.11)$$

The proton, neutron and mixed variance of the colliding particle respectively are stated as;

$$\sigma_{NN}^2(t) = \overline{\left(N_1^{\lambda} - \overline{N_1^{\lambda}}\right)^2}, \quad (3.12)$$

$$\sigma_{ZZ}^2(t) = \overline{\left(Z_1^{\lambda} - \overline{Z_1^{\lambda}}\right)^2}, \quad (3.13)$$

$$\sigma_{NZ}^2(t) = \overline{\left(N_1^{\lambda} - \overline{N_1^{\lambda}}\right)\left(Z_1^{\lambda} - \overline{Z_1^{\lambda}}\right)}. \quad (3.14)$$

Using the Langevin equation that is shown in Eq. 3.9, and taking the mean of the cluster, one can find the time evolution of the variances as follows;

$$\frac{\partial}{\partial t}\sigma_{NN}^2 = 2\frac{\partial \mathrm{v}_n}{\partial N_1}\sigma_{NN}^2 + 2\frac{\partial \mathrm{v}_n}{\partial Z_1}\sigma_{NN}^2 + 2D_{NN}, \tag{3.15}$$

$$\frac{\partial}{\partial t}\sigma_{ZZ}^2 = 2\frac{\partial \mathrm{v}_p}{\partial Z_1}\sigma_{ZZ}^2 + 2\frac{\partial \mathrm{v}_p}{\partial N_1}\sigma_{NZ}^2 + 2D_{ZZ}, \tag{3.16}$$

$$\frac{\partial}{\partial t}\sigma_{NZ}^2 = \frac{\partial \mathrm{v}_p}{\partial N_1}\sigma_{NN}^2 + \frac{\partial \mathrm{v}_n}{\partial Z_1}\sigma_{ZZ}^2 + \sigma^2{}_{NZ}\left(\frac{\partial \mathrm{v}_p}{\partial Z_1} + \frac{\partial \mathrm{v}_n}{\partial N_1}\right). \tag{3.17}$$

These coupled equations for proton and neutron distributions can be found in deep inelastic heavy ion collisions from Fokker-Planck equation. In addition to the diffusion coefficients (D_{NN} and D_{ZZ}), derivatives of the drift coefficients (v_p and v_n) are needed to obtain the variances from Eqns. 3.15, 3.16, and 3.17.

3.2 Quantal Diffusion Coefficients

Considering the stochastic parts of the drift coefficients where their mean values are zero, the quantal diffusion coefficients becomes

$$D_{\alpha\alpha}(t) = \int_0^t dt' \overline{\delta v_\alpha^\lambda(t)\delta v_\alpha^\lambda(t')}. \tag{3.18}$$

where $\delta v_\alpha^\lambda(t)$ is the stochastic part of the drift coefficients consisting of the fluctuations of the current density, and it is shown as;

$$\delta v_\alpha^\lambda(t) = \frac{\hbar}{m}\int d^3r g(x') \sum_{ij\in\alpha} \mathrm{Im}\left[\phi_j^* \alpha(\vec{r},t)\hat{\mathrm{e}}\cdot\vec{\nabla}\phi_i^\alpha(\vec{r},t)\delta\rho_{ji}^\lambda\right]. \tag{3.19}$$

To compute Eq. 3.19, both the particle set and hole states should be considered. Applying the primary principle of the SMF theory which states that the density matrix elements should be individual random numbers,

$$\overline{\rho_{ij}^\lambda} = \overline{\langle i\,|\rho_a^\lambda(t_0)|\,j\rangle} = \delta_{ij}n_j. \tag{3.20}$$

The use of this approach provides that one can only consider the occupied states instead of employing the unoccupied states. The diffusion coefficient is formulated as;

$$\begin{aligned} D_{\alpha\alpha}(t) &= \int_0^t dt' \overline{\delta v_\alpha^\lambda(t) \delta v_\alpha^\lambda(t')} \\ &= \int_0^t dt' \, \mathrm{Re} \left[\sum_{p\in P,\ \mathrm{h}\in \mathrm{T}} A_{ph}^\alpha(t) A_{ph}^*(t') + \sum_{p\in T,\ \mathrm{h}\in P} A_{ph}^\alpha(t) A_{ph}^*(t') \right]. \end{aligned} \tag{3.21}$$

where, p and h symbols indicate particle and hole states, respectively. The symbols P and T show projectile and target systems, respectively.

Also, in the Eq. 3.21, the particle-hole matrix representation is given by,

$$\begin{aligned} A_{ph}^\alpha(t) &= \frac{\hbar}{2m} \int d^3 r g(x') \left(\Phi_p^{*\alpha}(\vec{r},t) \hat{e} \cdot \vec{\nabla} \Phi_h^\alpha(\vec{r},t) - \Phi_h^\alpha(\vec{r},t) \hat{e} \cdot \vec{\nabla} \Phi_p^{*\alpha}(\vec{r},t) \right) \\ &= \frac{\hbar}{m} \int d^3 r g(x') \, \Phi_p^{*\alpha}(\vec{r},t) \left(\hat{e} \cdot \vec{\nabla} \Phi_h^\alpha(\vec{r},t) - \frac{x'}{2\kappa^2} \Phi_h^\alpha(\vec{r},t) \right). \end{aligned} \tag{3.22}$$

The calculation of Eq. 3.22, is not possible at this stage, but by using the hole-hole matrix representation, a complete set of projectile nuclei can be written as

$$\sum_{p\in P, h\in T} A_{ph}^\alpha(t) A_{ph}^{*\alpha}(t') = \sum_{a\in P, h\in T} A_{ah}^\alpha(t) A_{ah}^{*\alpha}(t') - \sum_{h'\in P, h\in T} A_{h'h}^\alpha(t) A_{h'h}^{*\alpha}(t'). \tag{3.23}$$

This kind of equation can be solved with the help of the completeness property [36] of the wave-function. The first term can not be eliminated using the integral property of wave functions because the wave functions contain different times. However, time-dependent single-particle wave functions behave approximately diabatically on short time intervals. Therefore, in the short time evolution $\tau = t - t'$, the time-dependent wave functions can be shifted forward and backward as;

$$\Phi_a(\vec{r},t') \approx \Phi_a(\vec{r} - \vec{u}\tau, t). \tag{3.24}$$

where, the time shift is $\tau = t - t'$, and the nucleon drift velocity is indicated as $\vec{u}(\vec{R},T)$ and depends on the mean position and the mean time. Then completeness property becomes

$$\sum_a \Phi_a^*(\vec{r}_1,t) \, \Phi_a(\vec{r}_2 - \vec{u}\tau, t) = \delta(\vec{r}_1 - \vec{r}_2 + \vec{u}\tau). \tag{3.25}$$

Using this property shown in Eq. 3.25, Eq. 3.23 becomes

$$\sum_{a\in P,h\in T} A^{\alpha}_{ah}(t)A^{*\alpha}_{ah}\left(t'\right) = \sum_{h\in T}\int d^3r_1 d^3r_2 \delta\left(\vec{r}_1-\vec{r}_2+\vec{u}_h\tau\right) W^{\alpha}_{h}\left(\vec{r}_1,t\right) W^{*\alpha}_{h}\left(\vec{r}_2,t'\right), \tag{3.26}$$

Thus, the sum over single particle states are eliminated and the calculations of quantal diffusion coefficient include only finite number hole states. It is found as [10],

$$\sum_{a\in T,h\in P} A^{\alpha}_{ah}(t)A^{*\alpha}_{ah}\left(t'\right) = \int d^3r\tilde{g}\left(x'\right) G_P(\tau) J^{P}_{\perp,\alpha}(\vec{r},t-\tau/2). \tag{3.27}$$

Finally, the proton and neutron diffusion coefficients are calculated in the form

$$\begin{aligned} D_{\alpha\alpha}(t) = &\int_0^t d\tau \int d^3r\tilde{g}\left(x'\right)\left[G_T(\tau)J^{T}_{\perp,\alpha}(\vec{r},t-\tau/2)+G_P(\tau)J^{P}_{\perp,\alpha}(\vec{r},t-\tau/2)\right] \\ &-\int_0^t d\tau\,\mathrm{Re}\left[\sum_{h'\in P,\ \mathrm{h}\in\mathrm{T}} A^{\alpha}_{h'h}(t)A^{*'}_{h'h}(t-\tau)+\sum_{h'\in T,\ \mathrm{h}\in P} A^{\alpha}_{h'h}(t)A^{*^{\alpha}}_{h'h}(t-\tau)\right]. \end{aligned} \tag{3.28}$$

The Eq. 3.28 consists of memory kernel $G_T(\tau)$, and it is given by,

$$G_T(\tau) = \frac{1}{\sqrt{4\pi}}\frac{1}{\tau_0}\exp\left[-\left(\tau/2\tau_0\right)^2\right]. \tag{3.29}$$

The magnitude of current densities that are perpendicular to the window plane is indicated as; $J^{T}_{\perp,\alpha}(\vec{r},t-\tau/2)$, and it is expressed as;

$$J^{T}_{\perp,\alpha}(\vec{r},t-\tau/2) = \frac{\hbar}{m}\sum_{h\in T}\left|\mathrm{Im}\,\Phi^{*\alpha}_{h}(\vec{r},t-\tau/2)\left(\hat{e}\cdot\vec{\nabla}\Phi^{\alpha}_{h}(\vec{r},t-\tau/2)\right)\right|. \tag{3.30}$$

The former term Eq. 3.28 provides the total number of nucleon currents through the systems. Relation with the Pauli blockage in nuclear reactions is indicated in the second term. From the formulated expression, one can understand that the quantal effects are related to the diffusion coefficients. The Eq.3.28 is a microscopic form and does not contain any free parameter. The integral over time corresponds to memory effects. It automatically include the Pauli blocking effect which has no classical counterpart. The summation is only over a finite number of occupied hole states (h) and these single-particle wave functions are obtained from TDHF solutions.

3.3 Quantal Drift Coefficients and Curvature Parameters

The drift coefficients need to be derived to calculate the covariances. It is not easy to derive the drift coefficients of the projectile-like or target-like fragments concerning the number of neutrons and protons as they pass through the TDHF window. A rough approximation can be made using the one-sided flux method.

In calculating the curvature parameters, the drift path of the projectile-like or target-like products at a given initial angular momentum, the change of the neutron and proton numbers with time, and the change of the neutron and proton diffusion coefficients with time are used. In MNT reactions, the light projectile-like products drift along the system isovector path by gaining or losing neutrons and then continue to drift along the iso-scalar path. This situation is given in idealized form in Fig.3.2. If the charge asymmetry $(N-Z)/A$ values of the colliding ions are equal or close, the net drift is zero and this approximation does not work. In this case, an asymmetric system with the same total mass number in the neighbor of the symmetric system with the same energy and the same orbital angular momentum is possible to approximately calculate the neutron and proton drift coefficients and hence the curvature parameters. The average values found in this way can be used for the main system.

From the time-dependent changes in the proton and neutron numbers, the direction (toward symmetry or asymmetry direction) of the drift can be specified. Using the drift information of the nucleons, the isoscalar and isovector curvature parameters are determined. These parameters are directly related to the potential energy surface.

The potential energy of the system as a function of the colliding nuclei is indicated $U(N_1, Z_1)$. The potential of the system is approximated into two parabolic expressions as follows

$$U\left(N_1, Z_1\right) = \frac{1}{2} a R_S^2 + \frac{1}{2} b R_V^2. \tag{3.31}$$

The first term in this expression corresponds to the isovector drift path perpendicular to the β-stability valley line and the second term corresponds to the isoscalar drift path along the β-stability valley line.

As stated earlier, to obtain the coupled differential equations, Eqns. 3.15, 3.16, and 3.17, the diffusion coefficients and derivatives of drift coefficients are needed. The diffusion coefficient part is covered in Sec. 3.2. For calculating the drift coefficients, the derivatives of the potential energy of the system due to nucleon numbers can be used with the help of Einstein's relation,

$$v_n(t) = -\frac{D_{NN}(t)}{T^*}\frac{\partial U(N_1, Z_1)}{\partial N_1}, \tag{3.32}$$

$$v_z(t) = -\frac{D_{ZZ}(t)}{T^*}\frac{\partial U(N_1, Z_1)}{\partial Z_1}. \tag{3.33}$$

Substituting Eq.3.31 to Eq.3.32 and Eq.3.33, the drift coefficients are written as;

$$v_n(t) = -D_{NN}(t)[-\alpha\ R_S \sin\phi + \beta\ R_V \cos\phi], \tag{3.34}$$

$$v_z(t) = -D_{ZZ}(t)[\alpha\ R_S \cos\phi + \beta\ R_V \sin\phi] \tag{3.35}$$

where the reduced curvature parameters are represented as $\alpha = a/T^*$ and $\beta = b/T^*$.

Due to Fig.3.2, the values of reduced curvature parameters α and β are calculated by using the following expressions:

$$\alpha = \frac{1}{\int_{t_1}^{t_2} R_S(t)dt}\int_{t_1}^{t_2}\left(\frac{v_n(t)\sin\phi}{D_{NN}(t)} - \frac{v_p(t)\cos\phi}{D_{ZZ}(t)}\right)dt\ . \tag{3.36}$$

$$\beta = \frac{1}{\int_{t_3}^{t_4} R_V(t)dt}\int_{t_3}^{t_4}\left(\frac{v_n(t)\cos\phi}{D_{NN}(t)} + \frac{v_p(t)\sin\phi}{D_{ZZ}(t)}\right)dt\ , \tag{3.37}$$

$R_V(t)$ and $R_S(t)$ are defined as $R_V(t) = n\cos\phi - z\sin\phi$ and $R_S(t) = z\sin\phi + n\cos\phi$ where n and z are defined as $n = N_0 - N_1$ and $z = Z_1 - Z_0$. The term $n\cos\phi - z\sin\phi$ is the distance of the point (N_1, Z_1) to the isovector path and the

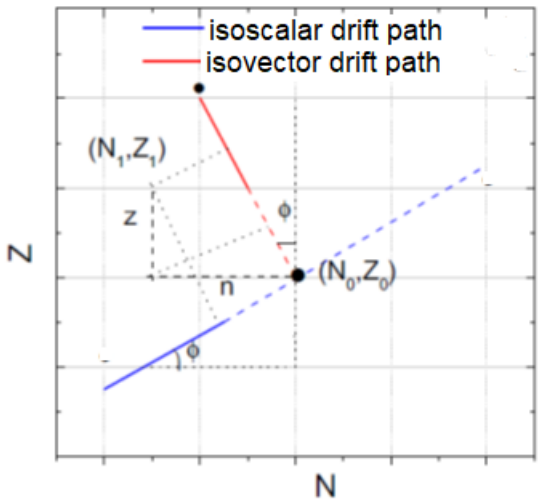


Figure 3.2: Illustration of isoscalar and isovector drift path.

term $z \sin\phi + n \cos\phi$ is the distance of the point (N_1, Z_1) to the isoscalar path. The averaged value of the isoscalar and isovector reduced curvature parameters over time integrals in the specified time intervals are chosen from drift path curves.

Thus, the derivatives of the drift coefficients are found in terms of the diffusion coefficients and the curvature parameters. In principle, it is possible to determine the derivatives of the curvature parameters and hence the drift coefficients from the average drift path calculated in the TDHF approach. However, this method does not work for systems with approximately the same initial charge asymmetries. In the case of the same initial charge asymmetry, neighboring asymmetric systems are used. The derivatives of the drift coefficients are found in terms of the diffusion coefficients and the curvature parameters as follows

$$\frac{\partial v_n}{\partial N_1} = -D_{NN}\left(\alpha \sin^2\phi + \beta \cos^2\phi\right), \tag{3.38}$$

$$\frac{\partial v_z}{\partial Z_1} = -D_{ZZ}\left(\beta \sin^2\phi + \alpha \cos^2\phi\right), \tag{3.39}$$

$$\frac{\partial v_n}{\partial Z_1} = -D_{NN}(\beta - \alpha)\cos\phi \sin\phi, \tag{3.40}$$

$$\frac{\partial v_z}{\partial N_1} = -D_{ZZ}(\beta - \alpha)\cos\phi \sin\phi. \tag{3.41}$$

In the Eq.3.15 and Eq.3.16, by using $\sigma_{NN}(t=0)=0$, $\sigma_{NZ}(t=0)=0$, and $\sigma_{ZZ}(t=0)=0$ the coupled differential equations can be solved. Then, using the computed quantal diffusion coefficients, the neutron and proton variances can be found.

In the ^{160}Gd+^{186}W system, the initial charge asymmetries for ^{160}Gd and ^{186}W are the same. We therefore study the neighbor ^{172}Gd$+^{174}$W system to calculate the isovector curvature parameter. For the calculation of the isoscalar curvature parameter β we consider the main system of ^{160}Gd + ^{186}W. In this system, there are two parts of the motion along the isoscalar path. The system may drift through the symmetry direction and then its direction change toward the asymmetry direction. Therefore, we should calculate the two βvalues as β^{sym} and β^{asym} corresponding to drift directions. In ^{160}Gd + ^{186}W system, nucleons first drift along the isoscalar line toward asymmetry or symmetry direction and then go back to inverse direction depending on the initial orientations. In this situation, two β values (β^{asym} andβ^{sym}) should be calculated and then their average value is taken as $\overline{\beta}$= (β^{sym}_{AB}+ β^{asym}_{BC})/2. Since ^{160}Gd and ^{186}W have the same initial asymmetry in the ^{160}Gd + ^{186}W system, in order to find the isovector curvature parameter, the neighbor asymmetric system ^{172}Gd$+^{174}$W is used. Detailed calculations are given in Sec.4.1.3.

$$\beta^{sym} = -\frac{1}{R_V^{sym}} \int_{t_A}^{t_B} \left(\frac{v_n(t)\cos\phi}{D_{NN}(t)} + \frac{v_p(t)\sin\phi}{D_{ZZ}(t)} \right) dt \ , \tag{3.42}$$

$$\beta^{asym} = \frac{1}{R_V^{asym}} \int_{t_B}^{t_C} \left(\frac{v_n(t)\cos\phi}{D_{NN}(t)} + \frac{v_p(t)\sin\phi}{D_{ZZ}(t)} \right) dt \ . \tag{3.43}$$

3.4 Cross-section of the Primary Products

The $P_\ell(N,Z)$ is indicated as the joint probability distribution function, and obtained with the output of the Langevin equations. The Langevin equations are the same as the Fokker-Planck equations from the view of the distribution of the macroscopic variables [37]. For each initial orbital angular momentum ℓ, the proton and neutron distribution function of projectile-like or target-like fragments are obtained by the proton, neutron and mixed dispersions as a correlated Gaussian function given by

$$P_\ell(N,Z) = \frac{1}{2\pi\sigma_{NN}(\ell)\sigma_{ZZ}(\ell)\sqrt{1-\rho_\ell^2}} \exp\left(-C_\ell\right). \tag{3.44}$$

where l represents the initial angular momentum. For each ℓ, C_l is given as

$$\begin{aligned} C_\ell =& \frac{1}{2\left(1-\rho_\ell^2\right)} \left[\left(\frac{Z-Z_\ell}{\sigma_{ZZ}(\ell)}\right)^2 - 2\rho_\ell \left(\frac{Z-Z_\ell}{\sigma_{ZZ}(\ell)}\right)\left(\frac{N-N_\ell}{\sigma_{NN}(\ell)}\right) \right. \\ & \left. + \left(\frac{N-N_\ell}{\sigma_{NN}(\ell)}\right)^2 \right]. \end{aligned} \tag{3.45}$$

where the correlation coefficient ρ_ℓ given by

$$\rho_\ell = \frac{\sigma_{NZ}^2(\ell)}{[\sigma_{ZZ}(\ell)\sigma_{NN}(\ell)]}. \tag{3.46}$$

The cross-section of hot and excited primary fragment production is calculated by using the following expression,

$$\sigma^S(N,Z) = \frac{\pi\hbar^2}{2\mu E_{c.m}} \sum_{l_{\min}}^{l_{\max}} (2l+1) P_l^S(N,Z). \tag{3.47}$$

where,

$$P_l^S(N,Z) = \frac{1}{2}\left[P_{l,pro}^S(N,Z) + P_{l,\mathrm{tar}}^S(N,Z)\right]. \tag{3.48}$$

Here, the sign of 'S' refers to the geometry of the collision, and μ indicates the reduced mass of both nuclei. The expressions of $P_{l,pro}^S(N,Z)$ and $P_{l,tar}^S(N,Z)$ refer to normalized production probabilities of projectile-like and target-like fragments at initial angular momentum ℓ. In Eq. 3.50, the factor of 1/2 is used so that the distribution can be normalized to unity. In this thesis, the calculation is carried out over the initial angular momenta range between l_{min} and l_{max} in the range that fits the angular acceptance of the detector. Also, Eq. 3.50 can be written by identifying only the mass number of fragments so that the expression shows the probability distribution of mass number,

$$P_l^S(A) = \frac{1}{2}\left[P_{l,pro}^S(A) + P_{l,\mathrm{tar}}^S(A)\right]. \tag{3.49}$$

Here, the probability distribution of mass number is obtained by constraining the total mass number as A=N+Z,

$$P^S_{l,tar}(A) = \frac{1}{\sqrt{2\pi}} \frac{1}{\sigma^S_{AA}(l)} \exp\left[-\frac{1}{2}\left(\frac{A - A^S_{l,tar}}{\sigma^S_{AA}(l)}\right)^2\right]. \tag{3.50}$$

Here, the mass variance is given by ${\sigma_{AA}}^2(l)$= ${\sigma_{NN}}^2(l)$+ ${\sigma_{ZZ}}^2(l)$+ $2{\sigma_{NZ}}^2(l)$.

A similar expression is applicable for projectile-like fragments,

$$P^S_{l,pro}(A) = \frac{1}{\sqrt{2\pi}} \frac{1}{\sigma^S_{AA}(l)} \exp\left[-\frac{1}{2}\left(\frac{A - A^S_{l,pro}}{\sigma^S_{AA}(l)}\right)^2\right]. \tag{3.51}$$

CHAPTER 4

RESULTS

In this chapter, we present our calculations for the reaction ^{160}Gd$+^{186}$W. In Sec. 4.1, the results of TDHF calculations for the system ^{160}Gd$+^{186}$W at E_{cm} = 502.6 MeV and E_{cm} = 461.9 MeV energies are given. Sec.4.2 represents the results of the SMF approach. In this work, both partners of the system are deformed isotopes between doubly closed shells of ^{132}Sn (with Z=50 and N=82) and ^{208}Pb (with Z=82 and N=126). The system of our work has large prolate deformations [17]. Therefore, one can understand the dependence of multinucleon reaction on the orientation of both partners. In the results, this property is referred to as the collision geometry. Taking the practical usage in Kedziora and Simenel paper [38], the initial orientation of the target and projectile deformation axis are in the axis of the beam X, and the perpendicular axis is denoted as Y. In this work, four different orientations are considered. They are labeled as tip-tip (XX), tip-side (XY), side-tip (YX), and side-side (YY). The first letter of the labels refer to the lighter collision partner of the reaction [38]. The synthesis of neutron-rich (around N=126) heavy nuclei with atomic number Z=70-88 are studied in this system. Only the primary mass distributions of fragments that produced in ^{160}Gd $+$ ^{186}W are calculated. Cooling of hot and excited products is not studied because there is no experiment about secondary production.

4.1 TDHF Results

In the system ^{160}Gd$+^{186}$W, the projectile-like and the target-like nuclei stick together, and contact each other, a multinucleon transfer occurs through the window between them. The compound nucleus is separated into two nuclei with different proton and

neutron number as a result of QF and IQF reactions.

4.1.1 Nucleon Transfer Rate due to Initial Conditions

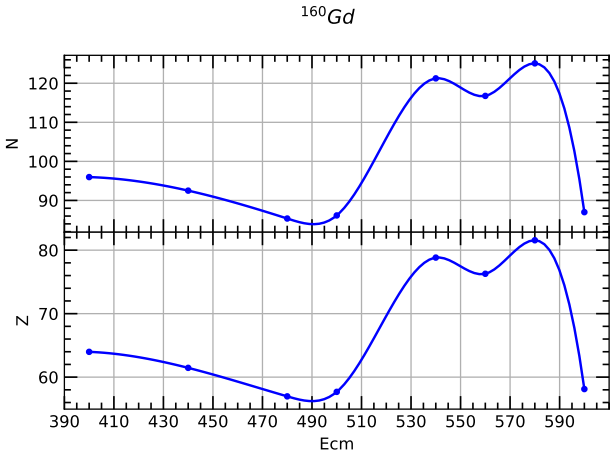
In this system, the projectile and the target nuclei are located between the closed-shell system of ^{132}Sn and ^{208}Pb. These closed shells should play an important role in the nucleon transfer process. While ^{160}Gd goes to ^{132}Sn, ^{186}W wants to go ^{208}Pb to be more stable. As a result a multinucleon transfer from the lighter projectile nuclei to the heavier target nuclei (IQF) occurs. To understand the effect of IQF, we investigate the nucleon transfer as a function of the center of mass energy (E_{cm}) and initial orientations. The Fig.4.1 represents the change of the ^{160}Gd and ^{186}W nuclei at different center of mass energies in tip-tip (XX) orientation.

In Fig.4.1, around the center of mass energy (E_{cm}) of the value E_{cm}=400 MeV, the collision is elastic, and there is almost no nucleon transfer in XX geometry. From the center of mass energy of E_{cm}=400 MeV to E_{cm}=500 MeV, the nucleon transfer is in the direction from the lighter nucleus (Gd) to heavier nucleus (W), and one can conclude for this case that the IQF is the dominant reaction. However, from the value of E_{cm}=500 MeV to E_{cm}=600 MeV, the transfer is from the heavier nucleus to the lighter, and the process for this transfer is the QF. After the value of E_{cm}=600 MeV, the nuclei may fuse, and produce a compound nucleus which will undergo fusion-fission process.

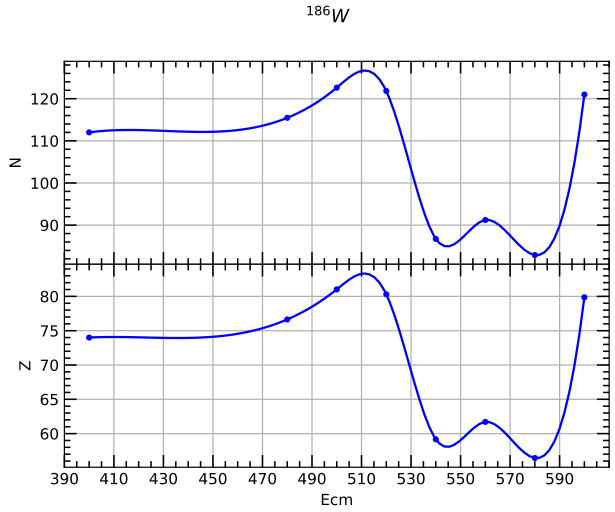
In the Fig.4.2, the evolution of the proton (Z) and neutron (N) numbers of the nucleus ^{160}Gd and ^{186}W nuclei at different center of mass energies in tip-side (XY) orientation is represented.

In Fig.4.2, the system at E_{cm}=400 MeV undergoes an elastic collision. Between E_{cm}=400 MeV and E_{cm}=520 MeV, the process is the IQF and between E_{cm}=550-600 MeV, the dominant process is QF.

In the Fig.4.3, the evolution of the proton (Z) and neutron (N) numbers of the nucleus ^{160}Gd and ^{186}W nuclei at different center of mass energies in side-tip (YX) orientation is represented.



(a)



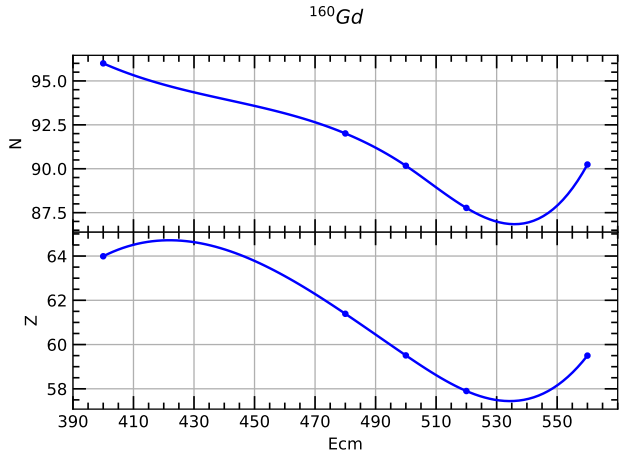
(b)

Figure 4.1: The evolution of the proton (Z) and neutron (N) numbers in terms of center of mass energy (E_{cm}), (a) for ^{160}Gd (b) for ^{186}W in tip-tip (XX) geometry.

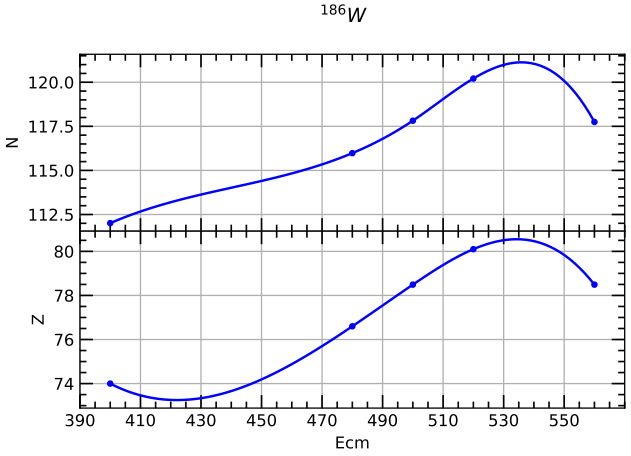
In Fig.4.3, one can see that at E_{cm}=400 MeV, the nucleon transfer does not exist. Between E_{cm}=400 MeV and E_{cm}=500 MeV, the nucleon transfer barely occurs, and after E_{cm}=500 MeV, the QF reaction occurs.

The Fig.4.4 shows the change of the proton (Z) and neutron (N) numbers of ^{160}Gd and ^{186}W in side-side (YY) geometry.

In Fig.4.4, the nucleon transfer is almost zero in the center of mass energy of E_{cm}=500



(a)

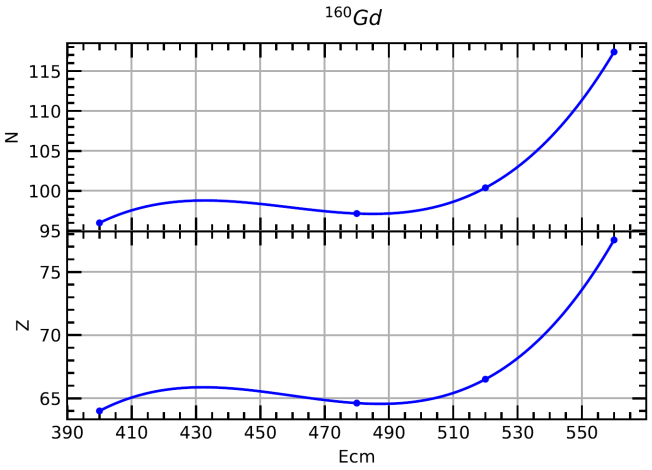


(b)

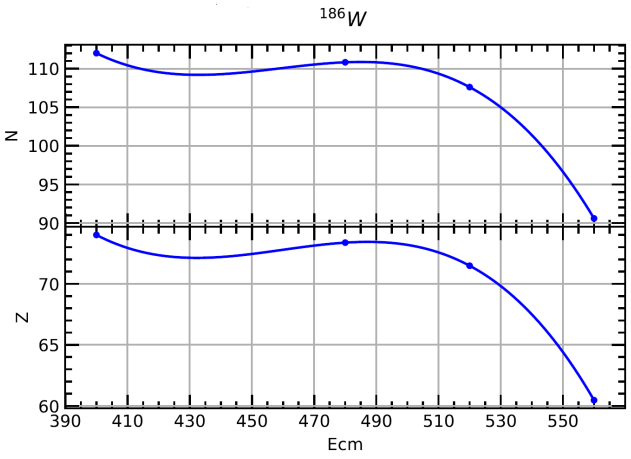
Figure 4.2: The evolution of the proton (Z) and neutron (N) numbers in terms of center of mass energy (E_{cm}). (a) for ^{160}Gd (b) for ^{186}W in tip-side (XY) geometry.

MeV. The graph shows that the nucleon transfer is from the heavier nucleus (W) to the lighter one (Gd) in all intervals, and the process is only the QF reaction.

The nucleon transfer rate is affected not only from the nucleon transfer rate but also from the center of mass energy. The nucleon transfer rate depends on the initial angular momentum of the projectile-like ion too. As an example we chose E_{cm}=461.9 MeV energy to investigate the effect of initial angular momentum on the nucleon exchange between ions. The change of proton and neutron numbers for ^{160}Gd and



(a)

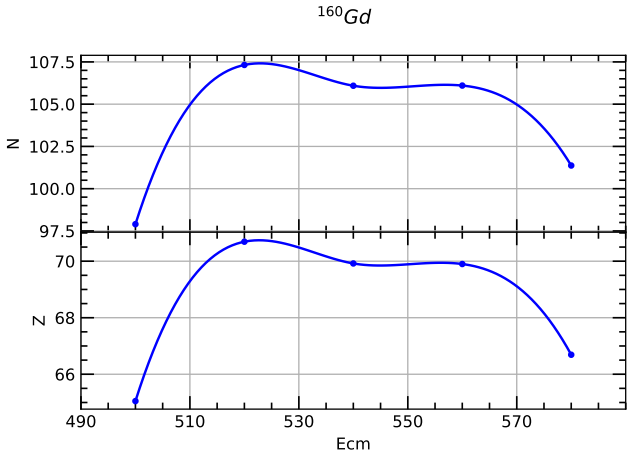


(b)

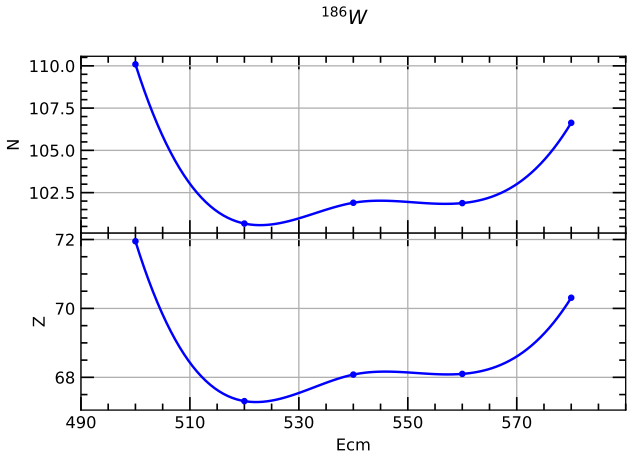
Figure 4.3: The evolution of the proton (Z) and neutron (N) numbers in terms of center of mass energy (E_{cm}), (a) for ^{160}Gd (b) for ^{186}W nuclei in side-tip (YX) geometry.

^{186}W nuclei are presented in Fig.4.5 at E_{cm}=461.9 MeV as a function of initial angular momentum ℓ in the tip-tip orientation of ^{160}Gd + ^{186}W system.

From Fig.4.5, we observed that the increasing angular momentum causes a decrease in the nucleon transfer rate. It is seen that for ℓ bigger than 100$\hbar$, QF (or IQF) disappears. Between 100$\hbar$ to 200$\hbar$, one or two nucleon transfers occur to equilibrate the asymmetry. For ℓ bigger than 200$\hbar$, a nucleon transfer does not take place which corresponds to pure elastic scattering.



(a)

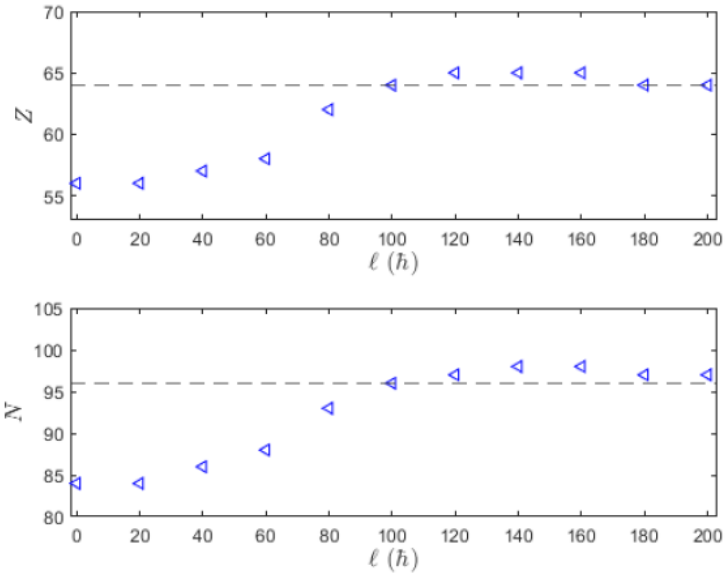


(b)

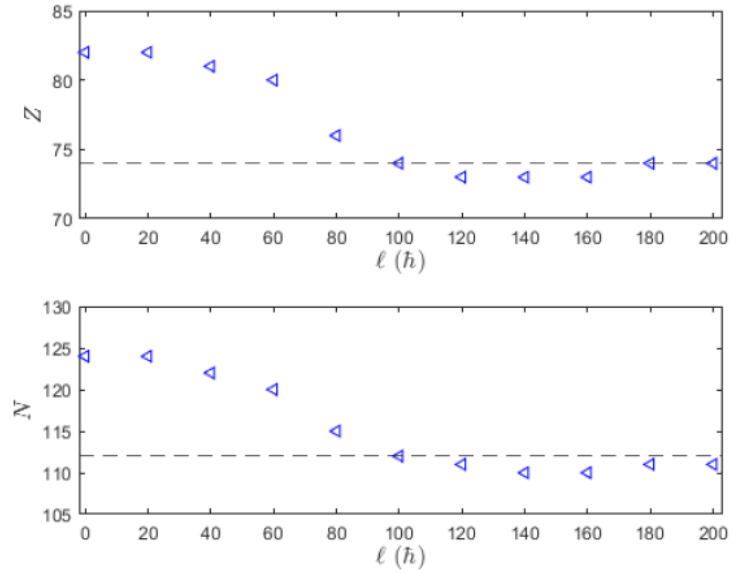
Figure 4.4: The evolution of the proton (Z) and neutron (N) numbers in terms of center of mass energy (E_{cm}), (a) for ^{160}Gd (b) for ^{186}W in side-side (YY) geometry.

4.1.2 The Calculation in ^{160}Gd + ^{186}W System

As well as the collision geometry, the placement of the fragments to the reaction box is also an important property for the reaction mechanism. Both ^{160}Gd and ^{186}W nuclei have prolate deformations. Four initial orientation geometries are taken: tip-tip (XX), tip-side (XY), side-tip (YX) and side-side (YY) in the calculation. The mass density profiles are plotted in four different geometries at different times of the window shown in Fig.4.6. The illustrations are presented as before and after



(a)



(b)

Figure 4.5: The evolution of the proton (Z) and neutron (N) numbers as a function of angular momentum ℓ for the nuclei (a) for ^{160}Gd (b) for ^{186}W nuclei.

separation in different time steps which are the beginning of the motion, creation of the initial neck, the creation of final neck, and separation into di-nuclear system.

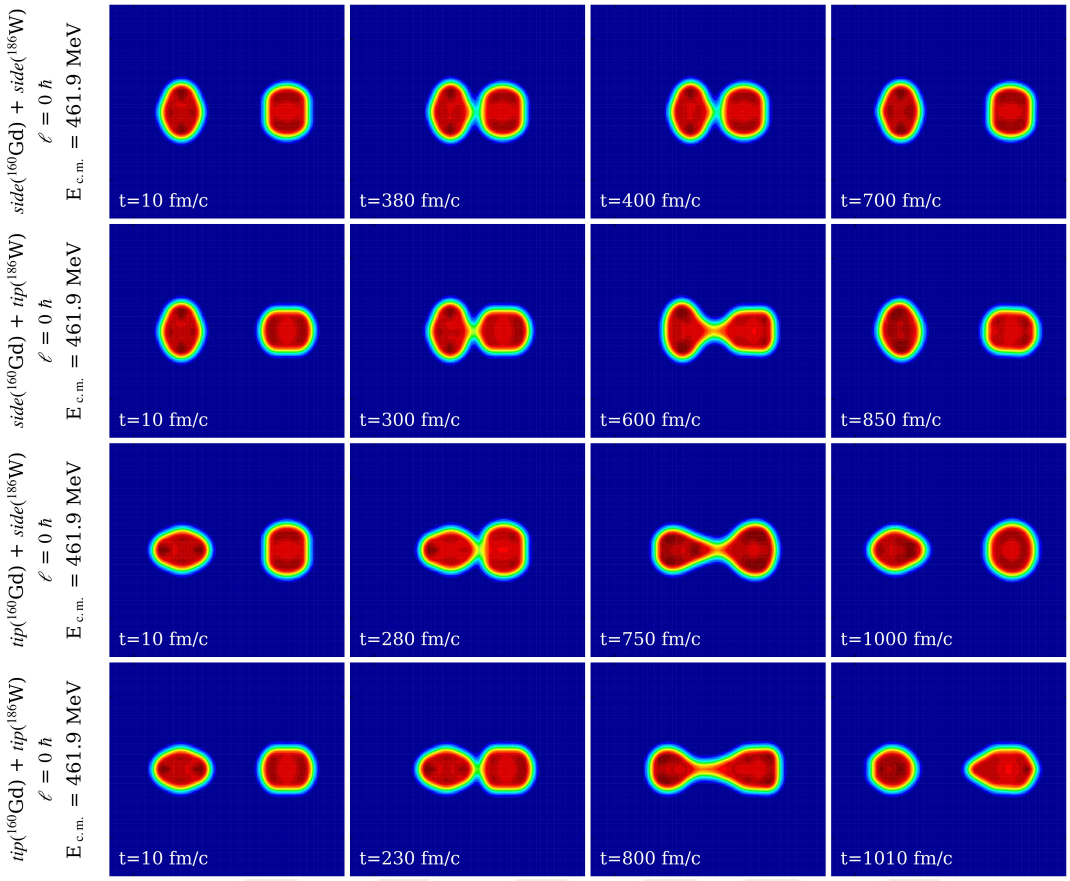


Figure 4.6: Snapshots of density profiles for different geometries at different times of the reaction mechanism.

Fig.4.6 shows the placement of the fragments and their deformations during the reaction. Fig.4.6 provides the contact time between the reaction partners during the transfer and separation, and it is clearly seen that the contact time between the partners are shorter in tip-tip geometry than the tip-side, side-tip, and the side-side geometries.

The calculations are done with the $3D$ TDHF code [39] by using the SLy4d Skyrme energy density functional with a finite-sized box of 60 x 60 x 36 fm in x, y and z directions [40]. The TDHF results are presented in the XX, XY, YX and YY geometries in Tab.4.1 for E_{cm}=502.6 Mev and in Tab.4.2 for E_{cm}=461.9 MeV energies. In the case of E_{cm}=461.9 MeV, we present only XX and XY geometries. YX and YY results are out of the experiment angular ranges. Tab. 4.1 and Tab. 4.2 contain initial angular momentum $\ell_i(\hbar)$, final mass and charge numbers of Gd-like fragments with A_1^f and Z_1^f and final mass and charge numbers of W-like fragments with A_2^f

and Z_2^f. The tables include the total kinetic energy lost (TKEL) in MeV units, in the center of mass scattering angle $\theta_{c.m.}$ and the laboratory scattering angles θ_1^{lab} and θ_2^{lab} of fragments in the lab frame calculated from following expressions,

$$\tan\theta_1^{\rm lab} = \frac{\sin\theta_{\rm c.m.}}{\sqrt{\frac{A_1^i A_1^f}{A_2^i A_2^f}\frac{E_{\rm cm}}{\rm TKE}} + \cos\theta_{\rm cmm}}, \tag{4.1}$$

and

$$\tan\theta_2^{\rm lab} = \frac{\sin\theta_{\rm cm}}{\sqrt{\frac{A_1^i A_2^f}{A_1^f A_2^i}\frac{E_{\rm cm}}{\rm TKE}} - \cos\theta_{\rm cm}}. \tag{4.2}$$

To decrease the computation period, the quantities are utilized in steps of twenty units of angular momentum. The range of initial angular momentum values is chosen in regards to the acceptance of the detector position in the experiment [17]. In the laboratory frame, the range of acceptance of the detector is 25°-65°.

In Tab. 4.2, for the ^{160}Gd + ^{186}W system at $E_{\rm cm} = 461.9$ MeV, the TDHF results are represented only in tip-tip (XX) and tip-side (XY) because only these geometries' products of the reaction fall in the acceptance range of the detectors.

4.1.3 Calculations of Drift Path and Reduced Curvature Parameters

The iso-scalar reduced curvature parameters β covered in Sec. 3.3 are calculated, and here initial angular momentum $\ell_i = 0\hbar$ for the system of ^{160}Gd + ^{186}W in all four orientations. The time intervals t_A, t_B and t_C shown in Fig.4.6 corresponds to the parts A, B and C presented in Fig.4.7 are used to calculate the iso-scalar reduced curvature parameter β. The changes of neutron and proton numbers of W-like fragments with time in four initial orientations are given in Fig.4.7 and, their drift paths along the isoscalar path in Fig.4.8.

In Fig. 4.7, the changes of the proton $Z(t)$ and neutron $N(t)$ numbers for W-like fragments are plotted for ℓ=0 for different collision orientations of the ^{160}Gd + ^{186}W system. To understand the proton and neutron transfers in the ^{160}Gd + ^{186}W system, the drift paths can be used.

Table 4.1: TDHF results for the ^{160}Gd + ^{186}W system at $E_{\rm cm}$ = 502.6 MeV in tip-tip (XX), tip-side (XY), side-tip (YX) and side-side (YY) geometries.

Geometry	ℓ_i ($\hbar$)	Z_1^f	A_1^f	Z_2^f	A_2^f	ℓ_f ($\hbar$)	$TKEL(MeV)$	$\theta_{c.m.}(deg.)$	$\theta_1^{lab}(deg.)$	$\theta_2^{lab}(deg.)$
	120	61.1	152.7	76.9	193.3	117.1	245.7	120.8	55.0	24.1
	140	64.2	160.5	73.8	185.5	125.2	237.0	114.3	51.1	27.6
	160	65.8	164.5	72.2	181.5	134.0	208.2	111.8	51.1	30.0
XX	180	65.5	164.0	72.5	182.0	120.8	173.5	111.7	53.4	31.0
	200	65.6	164.3	72.4	181.7	138.0	140.5	107.5	53.2	33.9
	220	65.2	163.5	72.8	182.5	165.9	114.7	102.8	52.2	36.6
	240	64.5	161.8	73.5	184.2	202.3	85.3	98.7	51.7	39.1
	120	61.2	152.6	76.8	193.4	116.9	212.3	120.8	57.9	24.9
	140	64.7	161.6	73.3	184.4	132.8	212.6	113.6	52.3	28.8
	160	65.4	163.3	72.6	182.7	136.9	186.0	110.6	52.3	31.1
	180	65.3	163.3	72.7	182.7	141.2	169.3	106.8	51.6	33.2
XY	200	65.3	163.3	72.7	182.7	154.1	155.3	102.6	50.3	35.5
	220	65.1	163.0	72.9	183.0	170.6	136.3	99.0	49.5	37.6
	240	64.9	162.3	73.1	183.7	191.2	113.8	96.1	49.0	39.6
	260	64.4	161.5	73.6	184.5	218.8	81.9	94.1	49.3	41.4
	120	66.3	166.3	71.7	179.6	98.1	177.3	123.2	57.5	26.0
	140	66.1	165.5	71.9	180.5	117.4	162.3	117.2	56.2	29.0
	160	65.8	164.7	72.2	181.3	130.8	146.4	112.6	55.3	31.4
YX	180	65.9	165.0	72.1	181.0	148.2	134.2	107.9	53.5	33.9
	200 ,	65.3	163.8	72.7	182.2	168.5	122.0	103.6	52.2	36.1
	220	64.5	162.1	73.5	183.9	186.0	101.8	100.4	51.8	37.9
	240	64.1	161.0	73.9	185.0	217.5	73.5	97.9	51.8	39.7
	120	64.1	159.8	73.9	186.2	106.7	123.1	125.7	64.7	25.4
	140	64.4	160.8	73.6	185.2	123.4	113.8	120.1	62.0	28.3
YY	160	64.6	161.5	73.4	184.5	141.2	105.6	115.0	59.6	30.9
	180	64.6	161.6	73.4	184.4	159.4	95.6	110.6	57.7	33.2
	200	64.4	161.4	73.6	184.6	175.4	81.4	106.9	56.3	35.3
	220	64.3	161.2	73.7	184.8	193.2	66.3	103.7	55.3	37.1

Table 4.2: TDHF results for the ^{160}Gd + ^{186}W system at $E_{\rm cm}$ = 461.9 MeV in tip-tip (XX) and tip-side (XY) geometries.

Geometry	ℓ_i ($\hbar$)	Z_1^f	A_1^f	Z_2^f	A_2^f	ℓ_f ($\hbar$)	$TKEL(MeV)$	$\theta_{c.m.}(deg.)$	$\theta_1^{lab}(deg.)$	$\theta_2^{lab}(deg.)$
XX	140	65.0	162.6	73.0	183.4	88.9	97.7	129.7	65.8	23.8
	160	64.9	162.7	73.1	183.3	116.1	81.4	123.3	63.7	27.1
	180	64.4	161.5	73.6	184.5	149.7	56.7	117.9	62.6	30.1
XY	140	64.6	161.8	73.4	184.2	117.2	75.2	126.3	66.0	25.7
	160	64.5	161.7	73.5	184.3	138.2	59.2	121.3	64.3	28.4

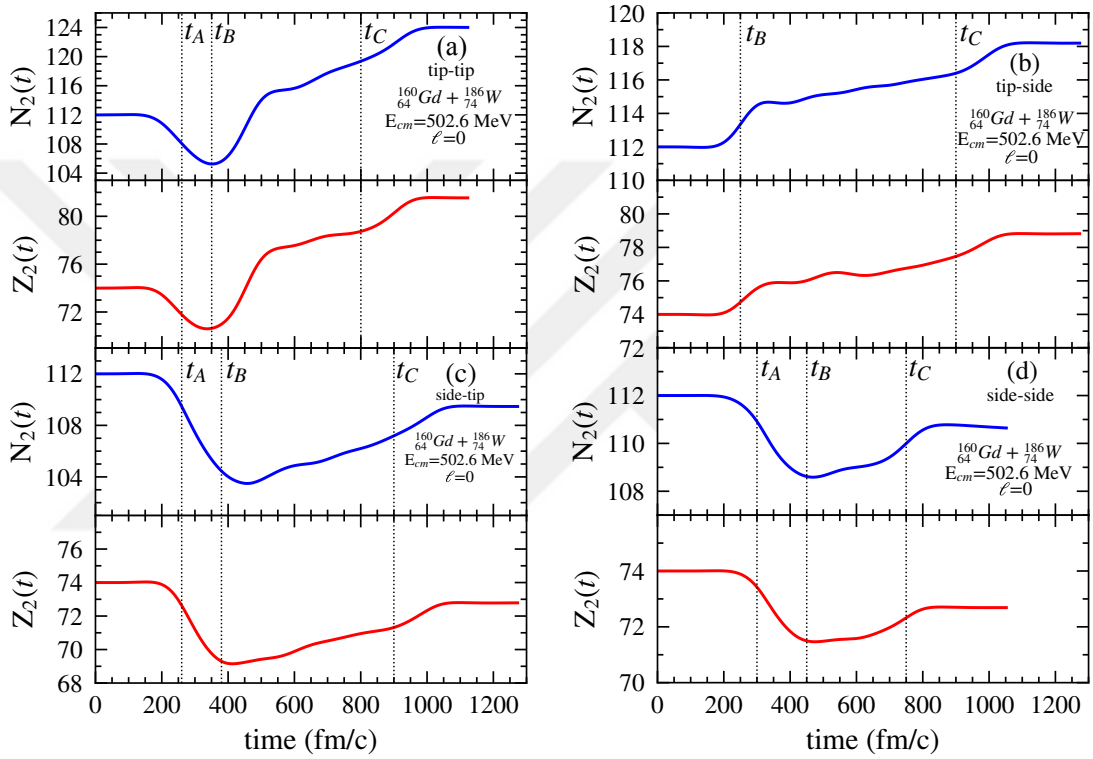


Figure 4.7: Mean values of proton and neutron numbers for W-like fragmenets in the head-on collision of the ^{160}Gd + ^{186}W system at $E_{\rm cm}$ = 502.6 MeV in tip-tip (a), tip-side (b), side-tip (c), and side-side (d) orientations. The figure was taken from Ref.[17]

By removing the time from the values of proton $Z(t)$ and neutron $N(t)$ numbers, the drift path is plotted in the (N, Z) plane for four initial orientation. The result of the drift path plotting is crucial because it gives an idea of the macroscopic properties of the reaction, and by virtue of the shell effect, all different geometries demonstrate different behavior.

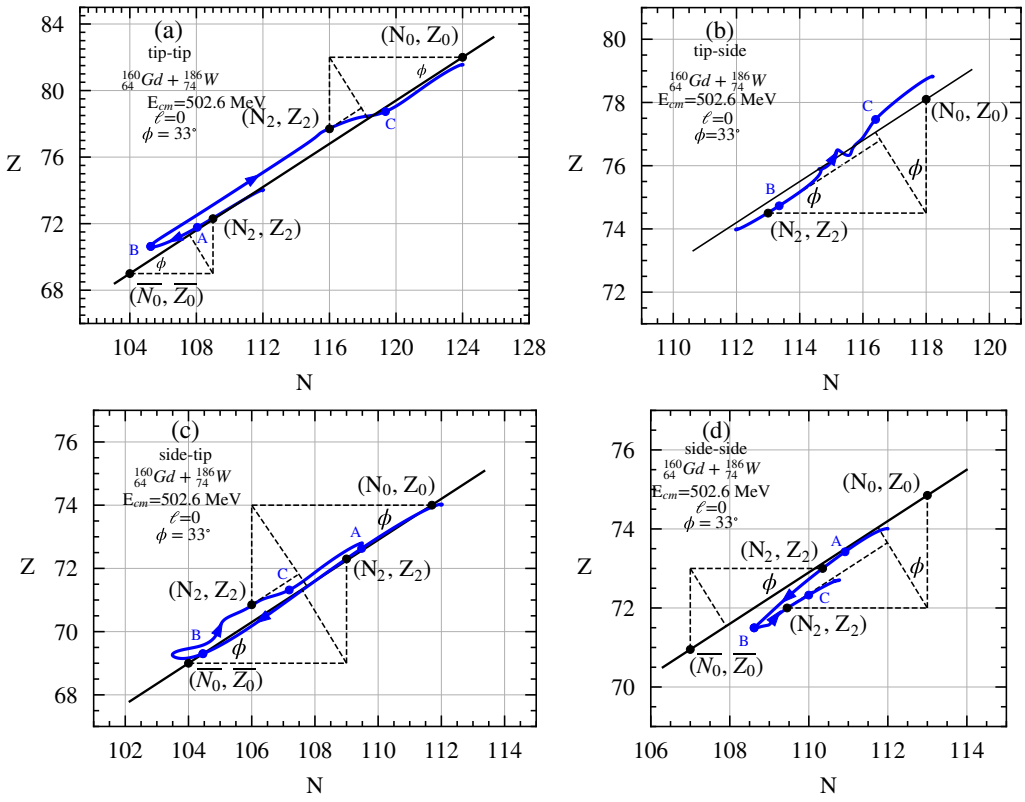


Figure 4.8: The drift path of W-like fragments in head-on collisions of the system ^{160}Gd + ^{186}W at $E_{\rm cm}$ = 502.6 MeV in tip-tip (a), tip-side (b), side-tip (c), and side-side (d) orientations. The figure was taken from Ref.[17]

In Fig. 4.8, the drift paths of head-on collisions of the system ^{160}Gd + ^{186}W at $E_{\rm cm}$ = 502.6 MeV for four different geometries are plotted. The W-like fragments of the drift path are shown with blue curves. The black lines show the partners of the reaction that have charge asymmetry value of $(N-Z)/(N+Z)$= 0.20 that are called the isoscalar path. This path goes near the bottom of the stability valley, and it stretches out from the lead area to the barium area making an angle of $\phi = 33°$ with a horizontal axis. In the ^{160}Gd + ^{186}W collision, the local equilibrium state in the heavier region is in the lead valley with the neutron and proton numbers N_0= 124 and Z_0=82, and the local equilibrium state in the lighter region is in the barium valley with N_0=84 and Z_0=56. These isotopes are on the isoscalar path with a charge asymmetry of 0.20. It is observed that there is a drift toward symmetry at first and then asymmetry in XX,

YX and YY initial orientations. In this system in particular, the W-like fragments in XX, XY geometries drift towards ^{208}Pb local equilibrium state in lead valley due to the closed shell effect Z=82. When there is drift in the asymmetry direction (toward Pb), the isoscalar distance is given by $R_V(t) = [N_0 - N_2(t)]\cos\phi + [Z_0 - Z_2(t)]\sin\phi$ and when there is drift in the symmetry direction (towards Ba valley), $\overline{R_V}(t) = [N_2(t) - \overline{N_0}(t)]\cos\phi + [Z_2(t) - \overline{Z_0}]\sin\phi$. Fig. 4.8 (a) states the drift path in tip-tip (XX) collision geometry. Here, the usual behavior of the QF reactions is that W-like fragments lose nucleons, and the system drifts to the symmetry. However, after the usual behavior occurs, the W-like fragments increase their nucleons and drift toward the asymmetry due to IQF reaction. In the case that is shown in Fig. 4.8 (b), the drift path of the tip-side (XY) is shown. Side-tip XY geometry also exhibits IQF. The side-tip (YX) collision is shown in Fig. 4.8 (c) and the drift path is similar to the XX collision. In YX collision, the heavy fragment starts losing nucleons and drifts towards the symmetry, but then shifts the direction to asymmetry. The collision of side-side (YY) geometry behaves in a similar manner to YX orientation. The isoscalar curvature parameter β is calculated from the following expressions in time intervals (t_A,t_B) and (t_B,t_C) as

$$\beta^{sym} = -\frac{1}{\int_{t_A}^{t_B} R_V(t)^{sym} dt} \int_{t_A}^{t_B} \left(\frac{v_n(t)\cos\phi}{D_{NN}(t)} + \frac{v_p(t)\sin\phi}{D_{ZZ}(t)} \right) dt \,, \tag{4.3}$$

$$\beta^{asym} = \frac{1}{\int_{t_B}^{t_C} R_V(t)^{asym} dt} \int_{t_B}^{t_C} \left(\frac{v_n(t)\cos\phi}{D_{NN}(t)} + \frac{v_p(t)\sin\phi}{D_{ZZ}(t)} \right) dt \,. \tag{4.4}$$

Table 4.3: Calculated curvature parameter β for the ^{160}Gd + ^{186}W system with $E_{\text{cm}} = 502.6$ MeV in tip-tip (XX), tip-side (XY), side-tip (YX) and side-side (YY) geometries. The time intervals between t_A and t_B are used to calculate the iso-scalar curvature parameters. The time values are in units of fm/c.

^{160}Gd + ^{186}W	t_A	t_B	t_C	β_{AB}^{sym}	β_{BC}^{asym}	$\beta = (\beta_{AB}^{sym} + \beta_{BC}^{asym})/2$
$Tip - tip$	260	350	800	0.010	0.034	0.022
$Tip - side$	-	250	900	-	0.008	0.008
$Side - tip$	260	380	900	0.016	0.004	0.010
$Side - side$	300	450	750	0.007	0.010	0.009

In Tab. 4.3, the computed iso-scalar curvature parameters β of the system ^{160}Gd + ^{186}W for four different orientations are presented. In the collisions of tip-tip, side-tip, and side-side geometries, first, the system drifts through the symmetry, and then the system starts to drift towards asymmetry. Here, the iso-scalar curvature parameters are obtained by taking the average of the values in the symmetry area and asymmetry part as $\beta = (\beta_{AB}^{sym} + \beta_{BC}^{asym})/2$.

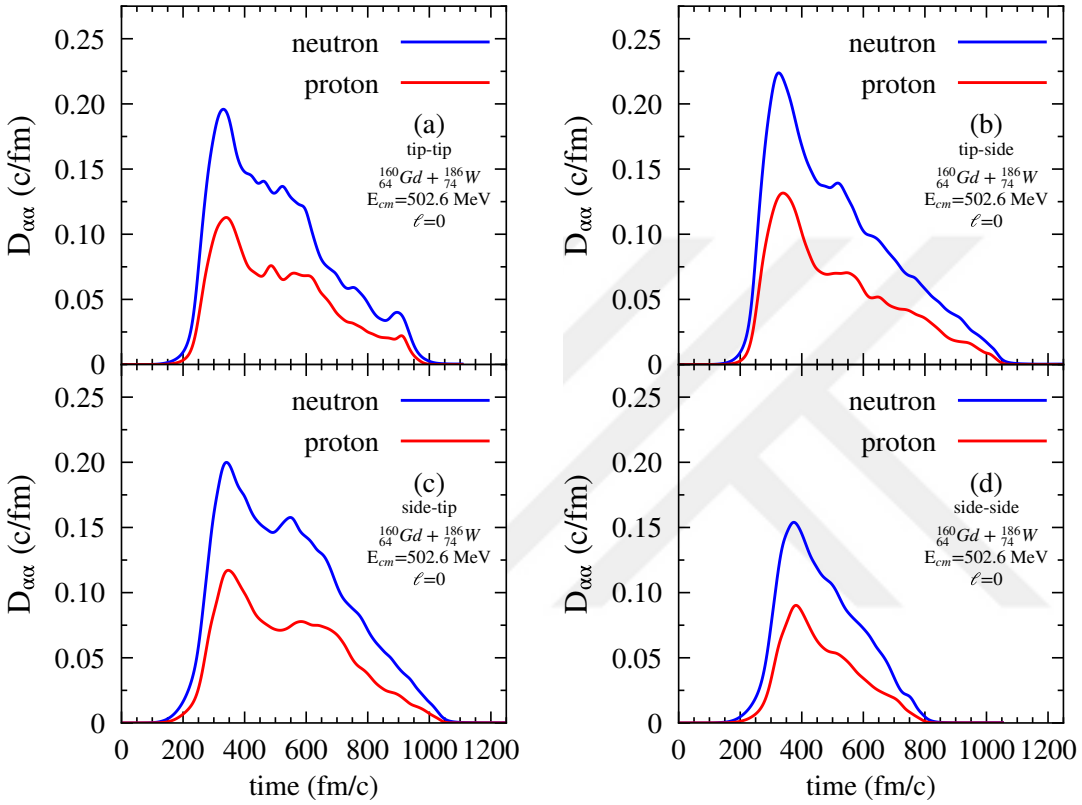


Figure 4.9: The neutron and proton diffusion coefficients of the ^{160}Gd + ^{186}W system at $E_{\text{cm}} = 502.6$ MeV in tip-tip (a), tip-side (b), side-tip (c), and side-side (d) geometries. The figure was taken from Ref.[17]

In Fig. 4.9, blue lines show the diffusion coefficients of neutron transfer, $D_{NN}(t)$, and the red lines indicate the diffusion coefficients of proton transfer, $D_{ZZ}(t)$ in the system ^{160}Gd + ^{186}W at $E_{\text{cm}} = 502.6$ MeV with initial angular momentum $\ell = 0\hbar$. As expected, the value of D_{NN} is bigger than the value of D_{ZZ}.

We consider the system of ^{172}Gd + ^{174}W at $E_{\text{cm}} = 502.6$ MeV energy which is the neighbor of ^{160}Gd + ^{186}W to calculate the isovector curvature parameter α.

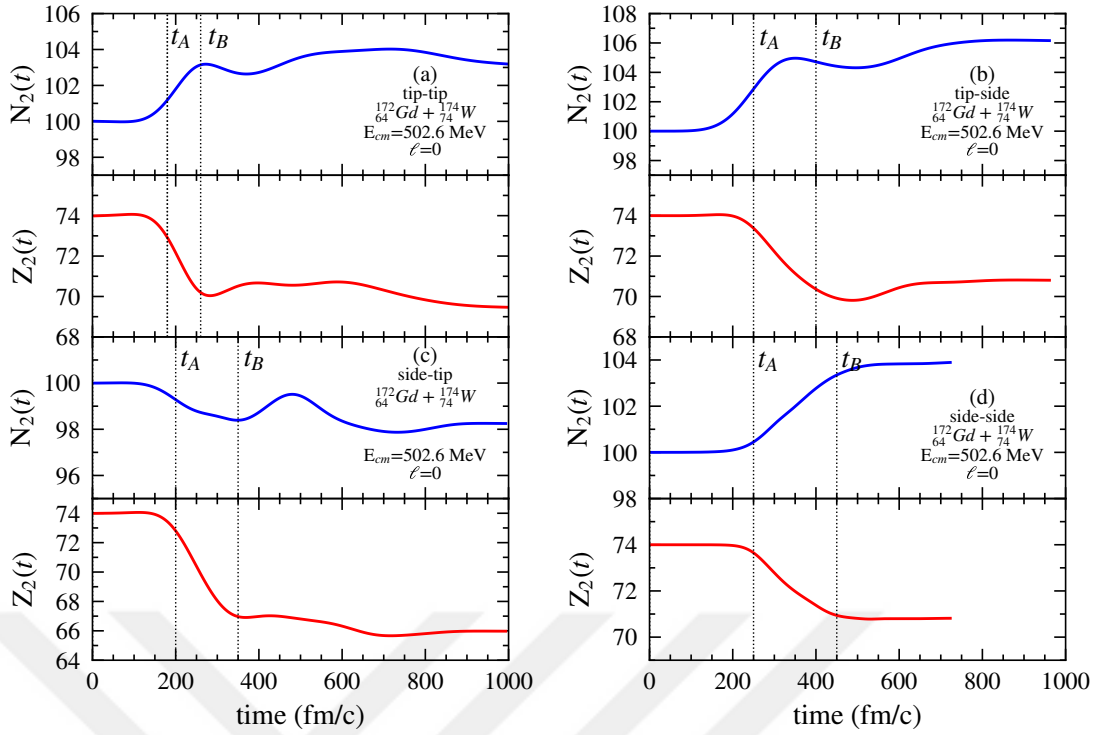


Figure 4.10: Mean values of proton and neutron numbers in the head-on collision of the ^{172}Gd + ^{174}W at $E_{\rm cm} = 502.6$ MeV in tip-tip (a), tip-side (b), side-tip (c), and side-side (d) orientations. The figure was taken from Ref.[17]

In Fig. 4.10, the change of the proton $Z(t)$ and neutron $N(t)$ numbers for W-like fragments in a time period are plotted. These plots are represented for different collision orientations of central collisions of the ^{172}Gd + ^{174}W system.

Fig. 4.11 shows the drift paths of the ^{172}Gd + ^{174}W system at $E_{\rm cm} = 502.6$ MeV in four different collision geometries. Here, the system drifts almost perpendicular to the stability valley which is named as iso-vector direction. The change in the iso-vector direction is influenced by the drift through the iso-scalar direction toward symmetry and asymmetry. After a short contact time, the fragments separate before the state of local equilibrium.

For the case of iso-vector curvature parameter α, we have used the ^{172}Gd + ^{174}W system at $E_{\rm cm} = 502.6$ MeV. In Tab. 4.4, the iso-vector curvature parameters α are calculated for different collision geometries by using

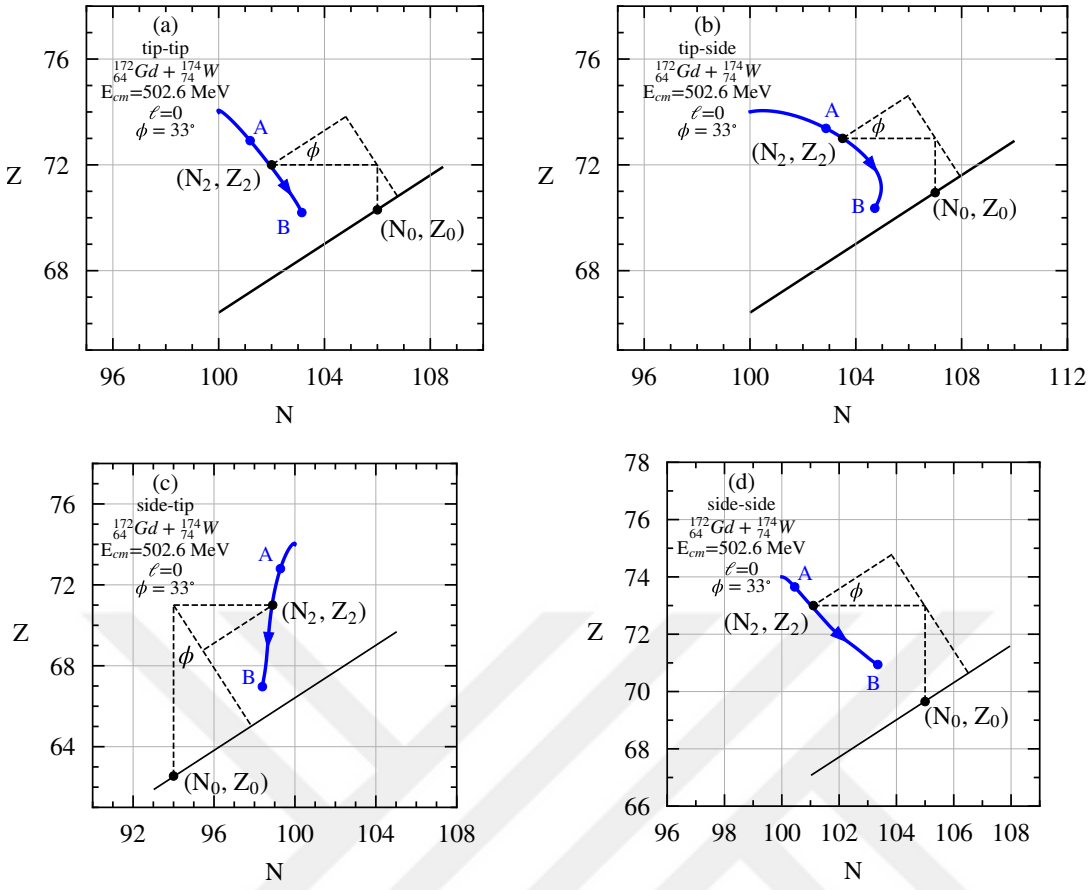


Figure 4.11: The drift path of W-like fragments in head-on collisions of the system ^{172}Gd + ^{174}W at $E_{\text{cm}} = 502.6$ MeV in tip-tip (a), tip-side (b), side-tip (c), and side-side (d) orientations. The figure was taken from Ref.[17]

$$\alpha = \frac{1}{\int_{t_A}^{t_B} R_S^{sym}(t)dt} \int_{t_A}^{t_B} \left(\frac{v_n(t)\sin\phi}{D_{NN}(t)} - \frac{v_p(t)\cos\phi}{D_{ZZ}(t)} \right) dt \ . \tag{4.5}$$

where the isovector distance is given by $R_S(t) = [N_0 - N_2(t)]\sin\phi - [Z_0 - Z_2(t)]\cos\phi$.

Finally, the curvature parameters are calculated with the help of the systems of ^{160}Gd+ ^{186}W and ^{172}Gd + ^{174}W reaction with $E_{\text{cm}} = 502.6$ MeV. The excitation energy does not affect the potential energy surface. Therefore, for the system of ^{160}Gd + ^{186}W with $E_{\text{cm}} = 461.9$ MeV, the curvature parameters are used as the same as with $E_{\text{cm}} = 502.6$ MeV.

In Fig. 4.12, the blue lines show the diffusion coefficients of neutron transfer, $D_{NN}(t)$, and the red lines indicate the diffusion coefficients of proton transfer, $D_{ZZ}(t)$ of the

Table 4.4: Calculated curvature parameter α using the system ^{172}Gd + ^{174}W reaction with $E_{\text{cm}} = 502.6$ MeV in tip-tip (XX), tip-side (XY), side-tip (YX) and side-side (YY) geometries. The time intervals between t_A and t_B are used to calculate the isovector curvature parameters. The time values are in units of fm/c.

^{172}Gd + ^{174}W	t_A	t_B	α
$Tip - tip$	180	260	0.113
$Tip - side$	250	400	0.133
$Side - tip$	200	350	0.127
$Side - side$	250	450	0.143

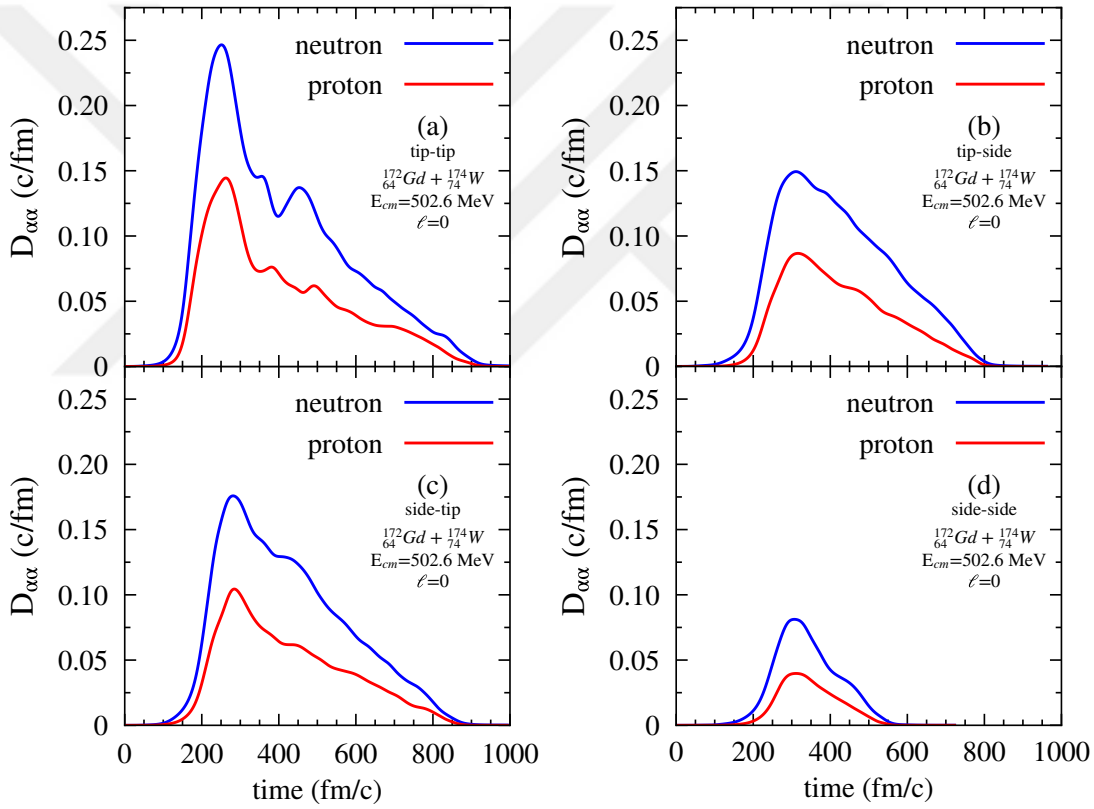


Figure 4.12: The neutron and proton diffusion coefficients of the system ^{172}Gd + ^{174}W at $E_{\text{cm}} = 502.6$ MeV in tip-tip (a), tip-side (b), side-tip (c), and side-side (d) geometries. The figure was taken from Ref.[17]

system ^{172}Gd + ^{174}W at E_{cm}=502.6 MeV with initial angular momentum $\ell = 0\hbar$. We use this graph with together Fig.4.10, Fig.4.11 to determine time intervals, t_A and t_B.

4.2 SMF Results

4.2.1 ^{160}Gd + ^{186}W System at $E_{\text{cm}} = 502.6$ MeV

To determine the neutron, proton, and mixed variances, the Eqns. 3.16, 3.17 and 3.18 are used with the computed curvature parameters and diffusion coefficients. The Tab.4.5 shows the results of σ_{NN} for neutrons, σ_{ZZ} for protons, σ_{NZ} for mixed dispersions, and σ_{AA} for mass variances. They are calculated for four different collision geometries tip-tip, tip-side, side-tip, and side-side.

Table 4.5: SMF results for the ^{160}Gd + ^{186}W reaction at $E_{\text{cm}} = 502.6$ MeV in tip-tip (XX) orientation.

Tip-tip (XX)					Side-tip (YX)				
ℓ_i(h)	σ_{NN}	σ_{ZZ}	σ_{NZ}	σ_{AA}	ℓ_i	σ_{NN}	σ_{ZZ}	σ_{NZ}	σ_{AA}
120	5.8	4.3	3.9	9.1	120	6.5	4.6	4.5	10.3
140	5.7	4.3	3.9	9.0	140	6.2	4.3	4.2	9.6
160	5.6	4.2	3.7	8.8	160	5.8	4.1	3.9	9.0
180	5.4	4.1	3.5	8.4	180	5.5	3.8	3.5	8.4
200	5.1	3.9	3.2	7.9	200	5.0	3.5	3.0	7.4
220	4.8	3.5	2.7	7.1	220	4.4	3.0	2.3	6.3
240	4.1	2.9	1.9	5.7	240	3.7	2.5	1.6	4.9
Tip-side (XY)					Side-side (YY)				
ℓ_i(h)	σ_{NN}	σ_{ZZ}	σ_{NZ}	σ_{AA}	ℓ_i	σ_{NN}	σ_{ZZ}	σ_{NZ}	σ_{AA}
120	7.1	4.9	5.2	11.3	120	5.4	3.7	3.5	8.3
140	6.9	4.8	5.0	11.0	140	5.1	3.5	3.3	7.7
160	6.6	4.5	4.7	10.4	160	4.8	3.3	2.9	7.2
180	6.2	4.3	4.3	9.7	180	4.5	3.1	2.6	6.5
200	5.9	4.1	4.0	9.1	200	4.0	2.8	2.1	5.7
220	5.4	3.8	3.5	8.3	220	3.6	2.4	1.6	4.8
240	4.8	3.4	2.9	7.1					
260	3.9	2.7	1.9	5.4					

Fig. 4.13 demonstrates the calculated neutron, proton, and mixed dispersions of the system ^{160}Gd + ^{186}W system at $E_{\rm cm} = 502.6$ MeV in tip-tip, tip-side, side-tip, and side-side geometries with the initial angular momentum $\ell = 0\hbar$. Fig. 4.13 shows that up to 400 fm/c, the magnitude orders of diffusions are $\sigma_{NN} > \sigma_{ZZ} > \sigma_{NZ}$. The order of the correlations changes over time inndicating the importance of correlations resulting the energy distribution. Note that σ_{NZ}= 0 in TDHF, hoowever, the magnitude of fluctuations in SMF give nonzero σ_{NZ}.

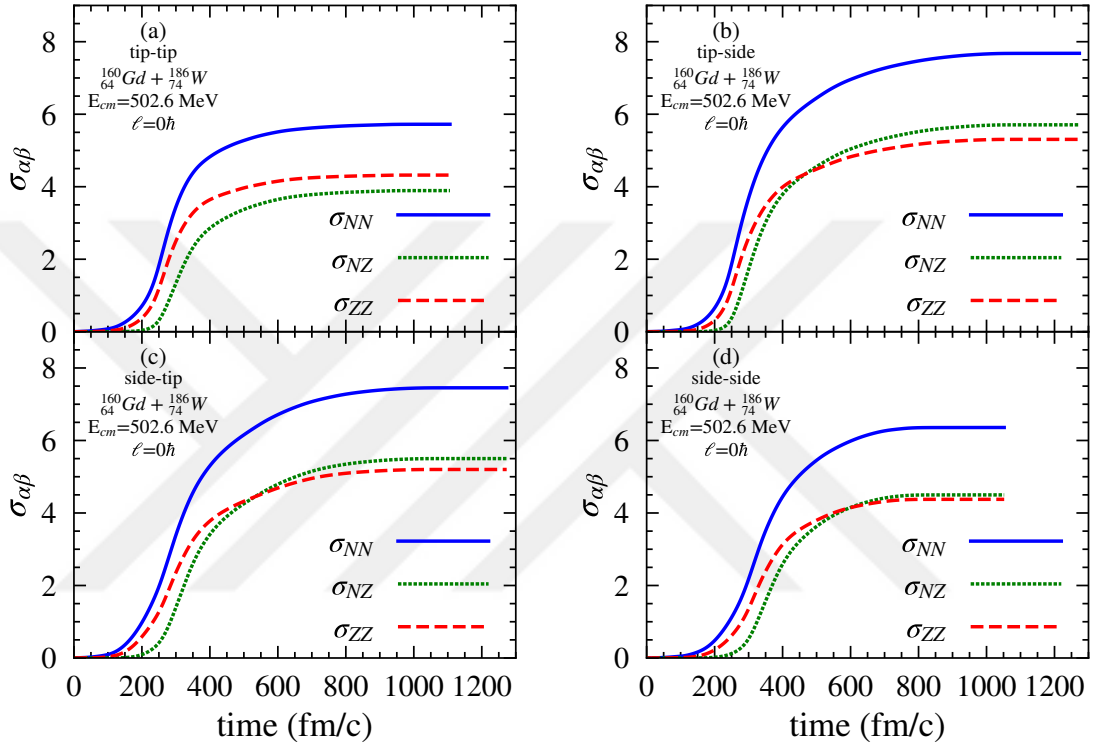


Figure 4.13: Neutron, proton, and mixed variances as a function of time in head-on collisions of the system ^{160}Gd + ^{186}W system at $E_{\rm cm} = 502.6$ MeV in tip-tip (a), tip-side (b), side-tip (c), and side-side (d) geometries. The figure was taken from [17].

In Fig. 4.14, the cross-section of the primary products of the ^{160}Gd + ^{186}W system at $E_{\rm cm} = 502.6$ MeV are presented in tip-tip, tip-side, side-tip, and side-side geometries as a function of the mass number.

The average cross-section as a function of mass number is shown with a solid black line. It is crucial that for the deformed nuclei, the effect of the orientation should be considered. To average these cross sections, it is necessary to take into account the effects of geometry of the deformed nuclei. When two orientations (tip and side) are

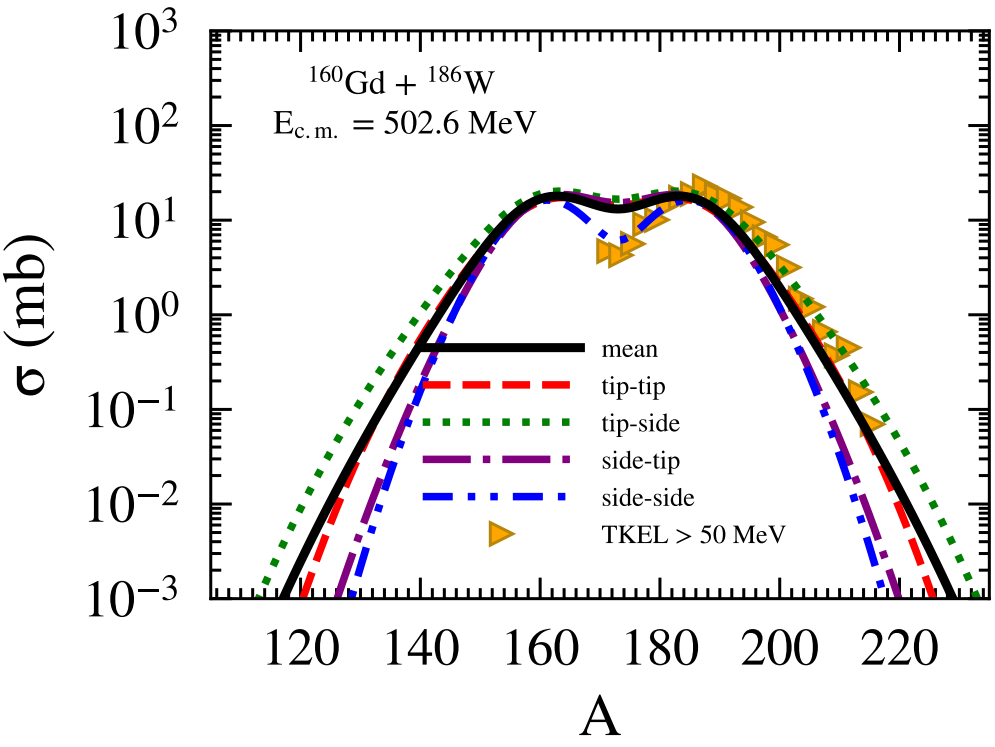


Figure 4.14: Total cross-sections of the system ^{160}Gd + ^{186}W system at $E_{\text{cm}} = 502.6$ MeV as a function of mass number A. The red dashed lines indicate the tip-tip, dotted-green lines tip-side, dashed-dotted purple lines side-tip, and dotted-dashed blue lines indicates the collision geometry of side-side reactions. Mean cross-section and experimental data are taken from Ref.[41] and are indicated by the solid black lines and yellow triangles, respectively. The figure was taken from Ref.[17]

considered, it is neccessary to define an angle separating the tip and side orienttaions. A method for the weighting between two orientation suggested by Hinde [42] are used in this thesis where critical angles are determined to separate the two orientations. For the energy E_{cm}=502.6 MeV, we choose the critical angle to be 37° and calculate the average values of orientations.

The cross-section of primary products of N= 126 isotones in ^{160}Gd + ^{186}W system at $E_{\text{cm}} = 502.6$ MeV is plotted as a function of proton number Z in Fig. 4.15. From Fig. 4.15, it is seen that the cross-section of the primary fragments in tip-side geometry is nearly one order of magnitude higher than the reactions in side-tip, and side-side. Therefore, this result emphasizes the effect of IQF in tip-side orientation.

The deformation and orientation of the collision fragments affect the reaction properties. It concludes that, unlike fusion-fission and fragmentation reactions, with the help of the MNT processes, neutron-rich heavy nuclei near the lead region can be synthesized.

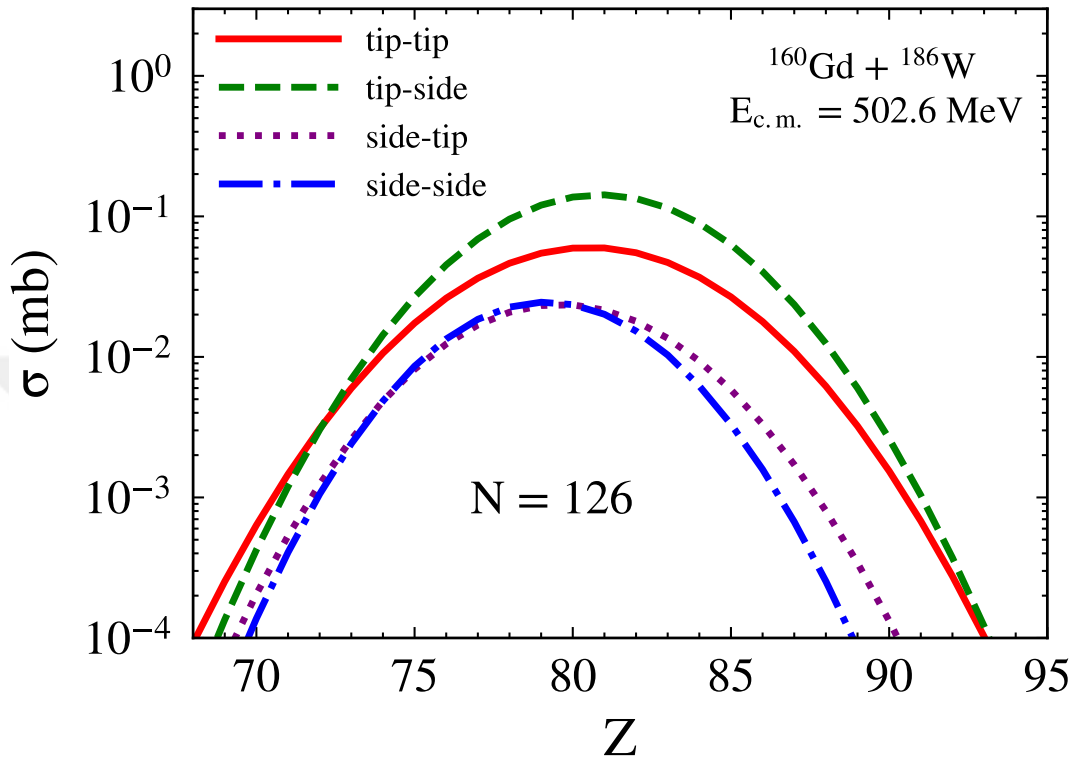


Figure 4.15: The cross-sections of primary products of the system ^{160}Gd + ^{186}W system at $E_{\text{cm}} = 502.6$ MeV. The figure was taken from Ref.[17].

4.2.2 ^{160}Gd + ^{186}W System at $E_{\text{cm}} = 461.9$ MeV

By using Eqs. 3.16, 3.17 and 3.18 with the computed curvature parameters and diffusion coefficients, the asymptotic values of dispersion are calculated. Tab. 4.6 shows the results of σ_{NN} for neutrons, σ_{ZZ} for protons, σ_{NZ} for mixed dispersions, and σ_{AA} for mass variances. They are calculated for two different collision geometries tip-tip, and tip-side. For this case, the results of only two different geometries are represented because the initial angular momentum values for side-tip and side-side do not fall into the acceptance range of the detectors.

Table 4.6: SMF results for the ^{160}Gd + ^{186}W reaction at $E_{\text{cm}} = 461.9$ MeV in tip-tip (XX) and tip-side (XY) geometries. The table was taken from Ref.[17]

$Geometry$	ℓ_i	σ_{NN}	σ_{ZZ}	σ_{NZ}	σ_{AA}
XX	140	5.1	3.8	3.1	7.7
	160	4.7	3.5	2.7	7.0
	180	4.1	3.0	2.0	5.8
XY	140	4.8	3.3	2.8	7.1
	160	4.3	3.0	2.3	6.1

In ^{160}Gd + ^{186}W system at $E_{\text{cm}} = 461.9$ MeV, the energy of the system is very close to the Bass barrier of 463.3 MeV. Therefore, the side geometries of collisions are suppressed because the system goes so close to the subbarrier regime [17]. The chosen critical angle need to be changed so that the weight of the tip geometry is increased. Therefore, for this case, the critical angle is chosen 60°. In Fig. 4.16, the total cross-section of the ^{160}Gd + ^{186}W at $E_{\text{cm}} = 461.9$ MeV as a function of mass number is shown. The results of side-tip and side-side geometries are not presented because their cross-sections are nearly zero. Therefore, the total cross-section calculations are done for the tip-tip and tip-side collision geometries. As presented in Fig. 4.16, the results give information that is compatible with the low-energy data shown in yellow circles. The results obtained in the quantal description show a good agreement with experimental data at both bombarding energies.

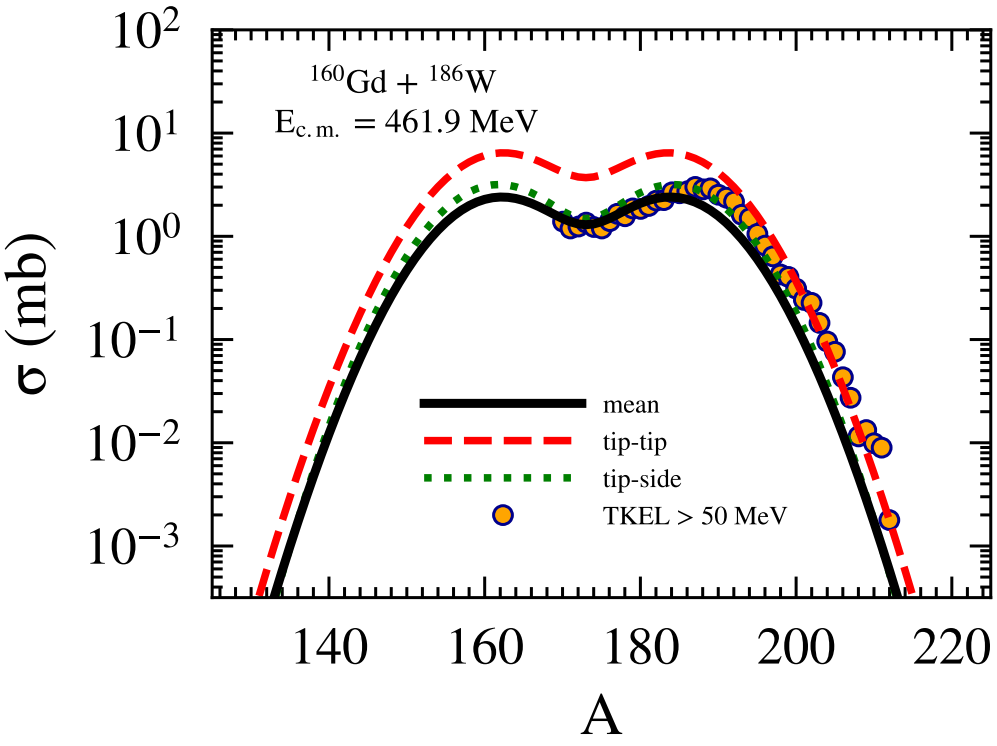


Figure 4.16: Total cross-section of the system ^{160}Gd + ^{186}W system at $E_{\text{cm}} = 461.9$ MeV as a function of mass number A. The red dashed lines represent the tip-tip, dotted-green lines tip-side. The figure was taken from [17]. Mean cross-section and experimental data are taken from Ref.[41] are indicated by the solid black lines and yellow circles, respectively. The figure was taken from Ref.[17].

CHAPTER 5

CONCLUSION

This thesis investigates the MNT reactions by using the TDHF theory and SMF approach. The emphasis of the investigation is the effect of the initial orientations of collision fragments on cross-section calculations of the primary fragment production. Also, the behavior of the QF and IQF processes at low energies near the Coulomb barrier of heavy ion collisions are determined. The quantal diffusion approach is used by employing the SMF approach to understand the nucleon transfer behavior. In this thesis, the HF and TDHF theories are briefly discussed. The SMF approach is explained briefly, and also the SMF results of ^{160}Gd + ^{186}W system reactions at two different bombarding energies are studied. First, the static properties of the reaction are determined by the HF theory. Once the partners are prepared as stationary, the fragments are ready for the dynamic part of the reaction. With the help of the single Slater determinant, the TDHF theory gives information on the dynamic part of the reaction. The single Slater determinant is used to calculate the single-particle density matrix. It is important to compute the transport description in terms of charge and mass asymmetry values. The description consists of the shell structure of the nuclei, the orientation of ions in the collision, and the Pauli exclusion principle. The macroscopic variables for computing the transport description of target-like fragments are chosen as the neutron and proton numbers. These variables are calculated by the linearized Langevin equations. After the collision of the target and the projectile nuclei, the product of the primary fragment distribution is determined with the Fokker-Planck equations. The single particle wave function of the TDHF method is utilized for approximating the diffusion coefficient. With the help of the drift path of the motion, the potential energy near the local equilibrium state is estimated. In the drift path of the reaction, the iso-scalar and iso-vector reduced curvature parameters are obtained with the neutron

and proton drift coefficient by using Einstein's relation. Also, the values of the mean values of proton and neutron numbers, and the proton, neutron, and mixed variances are computed. The probability distribution of the primary fragments is calculated with a Gaussian function. Finally, the cross-section of the primary products is found as a function of mass number. The results are compared with the experimental data provided by the paper [41]. The results represent a good description of both systems.

The ^{160}Gd + ^{186}W system is analyzed in terms of i) the bombarding energy, and ii) orientation of the reaction fragments. The system ^{160}Gd + ^{186}W is studied at E_{cm} = 502.6 MeV, and at E_{cm} = 461.9 MeV energies. In the case of E_{cm} = 502.6 MeV, the TDHF results are presented in terms of the geometries of tip-tip (XX), tip-side (XY), side-tip (YX) and side-side (YY). We have seen that the system with XX orientation begins the motion by demonstrating the usual QF process as the light fragment gains nucleon and the heavier fragment loses nucleon. However, after a time period that the QF reaction occurs, the system starts to exhibit IQF as the heavier one starts to gain nucleons and the lighter one starts to lose nucleons. In XY geometry, the system demonstrates the IQF reaction as well. For the systems with orientations YX and YY, the unusual type of behavior happens, and the system experiences the IQF reaction. This kind of reaction is a powerful tool to synthesize unknown neutron-rich isotopes and SHE. The effects of the collision geometries are shown in a wide range of initial angular momentum. Here, the range of the initial momentum ℓ is determined according to the position of the detectors in the laboratory frame. We have used the values that compatible with the angular acceptance of the detectors. In this work, the detectors' range of the acceptance is taken as 25° - 65°. The primary fragments production of the system ^{160}Gd + ^{186}W is studied at E_{cm} = 502.6 MeV in all four geometries falls into the range of the acceptance range of detectors. The total cross-section of primary products is plotted, and compared with the experimental data. The results provide a good description of experimental data. The iso-scalar calculation is determined with the drift path of the system and presented for four different orientations. The proton, neutron, and mixed variances are computed in four different geometries. With the help of these variances and covariances, the probability distribution of the mass number of the products can be obtained. Also, the cross-section of primary products for N=126 isotones is calculated. It is known that neutron-rich N=126 frag-

ments have a huge impact on astrophysics [43]. Therefore, it is clearly shown that the MNT mechanism is a powerful and useful tool for synthesizing neutron-rich heavy nuclei near the lead region.

The ^{160}Gd + ^{186}W system is analyzed at E_{cm} = 461.9 MeV as well. For this case, two orientations are used as tip-tip (XX) and tip-side (XY). The orientations of side-tip (YX) and side-side (YY) are not used since none of the initial angular momentum is in the range of the acceptance of detectors. The total cross-section of this system is calculated with XX and XY orientations only, and the results are found compatible with the experimental data.

The neighboring ^{172}Gd + ^{174}W system at $E_{\text{cm}} = 502.6$ MeV is studied for the isovector α calculation. In the calculations, the diffusion coefficients of the ^{172}Gd+^{174}W system calculated for four different geometries.

MNT mechanism is QF and IQF reaction of ^{160}Gd + ^{186}W system at E_{cm}=502.6 MeV and E_{cm} = 461.9 MeV are studied in the SMF approach. In addition to quantal diffusion approach, the first and second derivatives of the potential energy surface with respect to neutron and proton numbers are discussed to determine isoscalar and isovector curvature parameters in terms of drift coefficients and diffusion coefficients with the help of Einstin relations.

The SMF approach with an extension of TDHF theory provides valuable information in heavy-ion reactions. The approximations in these theories are used to build the nuclear reaction frame. Therefore, these methods and approaches contribute to future research.

REFERENCES

[1] O. R. Smits P. Schwerdtfeger and P. Pyykkö. The periodic table and the physics that drives it. *Nature Reviews Chemistry*, 4:359–380, 2020.

[2] G. Fea. Tabelle riassuntive e bibliografia delle trasmutazioni artificiali. *Il Nuovo Cimento*, 12:368–406, 1935.

[3] Mateusz Sitarz. *Research on production of new medical radioisotopes with cyclotron*. PhD thesis, University of Warsaw, 2019.

[4] V. Gopalakrishnan. *Physics of Nuclear Reactors*, pages 1–86. Elsevier, 2021.

[5] Hiroyuki Koura, Takahiro Tachibana, Masahiro Uno, and Masami Yamada. Nuclidic mass formula on a spherical basis with an improved even-odd term. *Progress of Theoretical Physics*, 113:305–325, 2005.

[6] Witold Nazarewicz. The limits of nuclear mass and charge. *Nature Physics*, 14, 2018.

[7] G. G. Adamian, N. V. Antonenko, A. Diaz-Torres, and S. Heinz. How to extend the chart of nuclides? *Eur. Phys. J. A*, 56:47, 2020.

[8] Kazuyuki Sekizawa and Sakir Ayik. Quantal diffusion approach for multinucleon transfer processes in the $^{58,64}\mathrm{Ni} + ^{208}\mathrm{Pb}$ reactions: Toward the production of unknown neutron-rich nuclei. *Phys. Rev. C*, 102:014620, 2020.

[9] S. Ayik, B. Yilmaz, O. Yilmaz, A. S. Umar, and G. Turan. Multinucleon transfer in central collisions of $^{238}\mathrm{U} + ^{238}\mathrm{U}$. *Phys. Rev. C*, 96:024611, 2017.

[10] S. Ayik, B. Yilmaz, O. Yilmaz, and A. S. Umar. Quantal diffusion description of multinucleon transfers in heavy–ion collisions. *Phys. Rev. C*, 97:054618, 2018.

[11] S. Ayik, B. Yilmaz, O. Yilmaz, and A. S. Umar. Quantal diffusion approach for multinucleon transfers in $\mathrm{Xe} + \mathrm{Pb}$ collisions. *Phys. Rev. C*, 100:014609, 2019.

[12] S. Ayik, O. Yilmaz, B. Yilmaz, and A. S. Umar. Heavy-isotope production in $^{136}\mathrm{Xe} + {}^{208}\mathrm{Pb}$ collisions at $E_{\mathrm{c.m.}} = 514$ MeV. *Phys. Rev. C*, 100:044614, 2019.

[13] Yu. Ts. Oganessian, V. K. Utyonkov, Yu. V. Lobanov, F. Sh. Abdullin, A. N. Polyakov, R. N. Sagaidak, I. V. Shirokovsky, Yu. S. Tsyganov, A. A. Voinov, G. G. Gulbekian, S. L. Bogomolov, B. N. Gikal, A. N. Mezentsev, S. Iliev, V. G. Subbotin, A. M. Sukhov, K. Subotic, V. I. Zagrebaev, G. K. Vostokin, M. G. Itkis, K. J. Moody, J. B. Patin, D. A. Shaughnessy, M. A. Stoyer, N. J. Stoyer, P. A. Wilk, J. M. Kenneally, J. H. Landrum, J. F. Wild, and R. W. Lougheed. Synthesis of the isotopes of elements 118 and 116 in the $^{249}\mathrm{Cf}$ and $^{245}\mathrm{Cm}{+}^{48}\mathrm{Ca}$ fusion reactions. *Phys. Rev. C*, 74:044602, Oct 2006.

[14] D. Kamas, A. Opichal, E. V. Chernysheva, S. N. Dmitriev, A. V. Gulyaev, A. V. Gulyaeva, M. Holik, J. Kliman, A. B. Komarov, L. Krupa, A. S. Novoselov, Yu. Ts. Oganessian, A. V. Podshibyakin, A. M. Rodin, V. S. Salamatin, S. V. Stepantsov, V. Yu. Vedeneev, and S. A. Yukhimchuk. Evaporation-residue cross sections in complete fusion reactions leading to Hg and Rn isotopes. *Phys. Rev. C*, 105:044612, 2022.

[15] E. Garrone, C.O. Areán, and B. Bonelli. How many chemical elements are there in the universe? *World Journal of Chemical Education*, 5:20–22, 2017.

[16] V. Zagrebaev and Walter Greiner. Production of heavy trans-target nuclei in multinucleon transfer reactions. *Physical Review C*, 87, 2013.

[17] S. Ayik, M. Arik, E. Erbayri, O. Yilmaz, and A. S. Umar. Multinucleon transfer mechanism in $^{160}\mathrm{Gd} + {}^{186}\mathrm{W}$ collisions in stochastic mean-field theory. *Phys. Rev. C*, 108:054605, 2023.

[18] A. B. Garrett. *The chemistry of elements 93, 94, 95 and 96 (Neptunium, Plutonium, Americium and Curium)*, volume 47. Ohio Journal of Science, 1947.

[19] B. Sharifi and D. Naderi. The effect of deformation and orientation of colliding nuclei on synthesis of superheavy elements. *Nuclear Physics A*, 991:121616, 2019.

[20] Roman Planeta. Physics of heavy ion collisions. *International Journal of Modern Physics E*, 15, 01 2012.

[21] Roger Balian and M Veneroni. Time-dependent variational principle for the expectation value of an observable: Mean-field applications. *Annals of Physics*, 281:65–142, 04 2000.

[22] B. Yılmaz O. Yılmaz and S. Ayik. Quantal diffusion in heavy-ion collisions. *ALKÜ Fen Bilimleri Dergisi*, pages 195–200, 2019.

[23] V. I. Zagrebaev and Walter Greiner. Production of heavy and superheavy neutron-rich nuclei in transfer reactions. *Phys. Rev. C*, 83:044618, Apr 2011.

[24] Valery Zagrebaev and Walter Greiner. Production of new heavy isotopes in low-energy multinucleon transfer reactions. *Phys. Rev. Lett.*, 101:122701, Sep 2008.

[25] E. M. Kozulin, G. N. Knyazheva, S. N. Dmitriev, I. M. Itkis, M. G. Itkis, T. A. Loktev, K. V. Novikov, A. N. Baranov, W. H. Trzaska, E. Vardaci, S. Heinz, O. Beliuskina, and S. V. Khlebnikov. Shell effects in damped collisions of $^{88}\mathrm{Sr}$ with $^{176}\mathrm{Yb}$ at the coulomb barrier energy. *Phys. Rev. C*, 89:014614, Jan 2014.

[26] C. Simenel and A. S. Umar. Heavy-ion collisions and fission dynamics with the time–dependent Hartree-Fock theory and its extensions. *Prog. Part. Nucl. Phys.*, 103:19–66, 2018.

[27] M. Arik, S. Ayik, O. Yilmaz, and A. S. Umar. Description of the multinucleon transfer mechanism for $^{48}\mathrm{Ca} + ^{244}\mathrm{Pu}$ and $^{86}\mathrm{Kr} + ^{198}\mathrm{Pt}$ reactions in a quantal transport approach. *Phys. Rev. C*, 108:064604, 2023.

[28] Emma Betty Suckling. *Nuclear structure and dynamics from the fully unrestricted Skyrme-Hartree-Fock model*. PhD thesis, University of Surrey, 2011.

[29] Kazuyuki Sekizawa. Tdhf theory and its extensions for the multinucleon transfer reaction: A mini review. *Frontiers in Physics*, 7, 2019.

[30] Kazuyuki Sekizawa. *Multinucleon Transfer Reactions and Quasifission Processes in Time-Dependent Hartree-Fock Theory*. PhD thesis, University of Tsukuba, 2015.

[31] R. Balian and M. Véneroni. Time-dependent variational principle for the expectation value of an observable: Mean-field applications. *Ann. Phys. (NY)*, 164:334, 1985.

[32] Kyle Godbey and A. S. Umar. Quasifission Dynamics in Microscopic Theories. *Front. Phys.*, 8:40, 2020.

[33] S. Ayik. A stochastic mean-field approach for nuclear dynamics. *Phys. Lett. B*, 658:174, 2008.

[34] D. Lacroix and S. Ayik. Stochastic quantum dynamics beyond mean field. *The European Physical Journal A*, 50, 2014.

[35] S. Ayik, K. Washiyama, and D. Lacroix. Fluctuation and dissipation dynamics in fusion reactions from a stochastic mean-field approach. *Phys. Rev. C*, 79:054606, 2009.

[36] S. Ayik, O. Yilmaz, B. Yilmaz, and A. S. Umar. Quantal nucleon diffusion: Central collisions of symmetric nuclei. *Phys. Rev. C*, 94:044624, 2016.

[37] Hannes Risken and Till Frank. *The Fokker–Planck Equation*. Springer–Verlag, Berlin, 1996.

[38] David J. Kedziora and Cédric Simenel. New inverse quasifission mechanism to produce neutron-rich transfermium nuclei. *Phys. Rev. C*, 81:044613, 2010.

[39] A. S. Umar, M. R. Strayer, J. S. Wu, D. J. Dean, and M. C. Güçlü. Nuclear Hartree-Fock calculations with splines. *Phys. Rev. C*, 44:2512–2521, 1991.

[40] A. S. Umar and V. E. Oberacker. Three-dimensional unrestricted time-dependent hartree-fock fusion calculations using the full skyrme interaction. *Phys. Rev. C*, 73:054607, 2006.

[41] E. M. Kozulin, V. I. Zagrebaev, G. N. Knyazheva, I. M. Itkis, K. V. Novikov, M. G. Itkis, S. N. Dmitriev, I. M. Harca, A. E. Bondarchenko, A. V. Karpov, V. V. Saiko, and E. Vardaci. Inverse quasifission in the reactions $^{156,160}\mathrm{Gd} + ^{186}\mathrm{W}$. *Phys. Rev. C*, 96:064621, 2017.

[42] D. J. Hinde, M. Dasgupta, J. R. Leigh, J. C. Mein, C. R. Morton, J. O. Newton, and H. Timmers. Conclusive evidence for the influence of nuclear orientation on quasifission. *Phys. Rev. C*, 53:1290–1300, Mar 1996.

[43] K. Zhao, Z. Liu, F.S. Zhang, and N. Wang. Production of neutron-rich n=126 nuclei in multinucleon transfer reactions: Comparison between 136xe + 198pt and 238u + 198pt reactions. *Physics Letters B*, 815:136101, 2021.